Publ. Astron. Soc. Japan (2017) 69 (1), R1 (1–35)
doi: 10.1093/pasj/psw103
Advance Access Publication Date: 2016 December 5
Invited Review

Invited Review

Rotation and mass in the Milky Way and spiral galaxies

Yoshiaki SOFUE[*]

Institute of Astronomy, The University of Tokyo, 2-21-1 Osawa, Mitaka, Tokyo 181-0015, Japan

[*]E-mail: sofue@ioa.s.u-tokyo.ac.jp

Received 2016 June 20; Accepted 2016 September 30

Abstract

Rotation curves are the basic tool for deriving the distribution of mass in spiral galaxies. In this review, we describe various methods to measure rotation curves in the Milky Way and spiral galaxies. We then describe two major methods to calculate the mass distribution using the rotation curve. By the direct method, the mass is calculated from rotation velocities without employing mass models. By the decomposition method, the rotation curve is deconvolved into multiple mass components by model fitting assuming a black hole, bulge, exponential disk, and dark halo. The decomposition is useful for statistical correlation analyses among the dynamical parameters of the mass components. We also review recent observations and derived results.

Key words: dark matter — galaxies: fundamental parameters — galaxies: kinematics and dynamics — galaxies: structure — Galaxy: fundamental parameters — Galaxy: kinematics and dynamics — Galaxy: structure

1 Introduction

Rotation of spiral galaxies is measured by spectroscopic observations of emission lines such as Hα, H I, and CO lines from disk objects, namely population I objects and interstellar gases. In these lines the velocity dispersion is negligibly small compared to rotational velocity, which implies that the pressure term is negligible in the virial theorem, so that the dynamical balance between the gravitational and centrifugal forces may be used to calculate the mass with sufficient accuracy. Absorption lines are also used for bulge kinematics using velocity dispersion and rotation. The dynamical approach is essential particularly for the measurement of the mass of the dark matter and black holes, which are not measurable via surface photometry assuming a mass-to-luminosity (M/L) ratio.

In sections 2 and 3 we review the various methods used to derive rotation curves of the Milky Way and of spiral galaxies, respectively, and describe the general characteristics of observed rotation curves. The progress in rotation curve studies is also briefly reviewed. In section 4 we review the methods used to determine the mass distributions in disk galaxies using the rotation curves, and describe their dynamical mass structures.

By definition, a rotation curve is the mean circular velocity around a nucleus as a single function of radius. Non-circular streaming motions, such as those due to spiral arms, bars, and/or expansion/contraction motions, are not considered here. The limitation of the current rotation curve analyses is discussed in section 2. Elliptical galaxies, of which rotation curve analysis is not applicable, are beyond the scope of this review. Considerations that employ unconventional physical laws, such as MOND (modified Newtonian dynamics), are also out of the scope of this review.

There are a number of articles and reviews on rotation curves and mass determination of galaxies, which

Table 1. Oort's constant *A* and *B*.

Source	*A* ($\mathrm{km\,s^{-1}\,kpc^{-1}}$)	*B* ($\mathrm{km\,s^{-1}\,kpc^{-1}}$)
Kerr and Lynden-Bell (1986)	14.4 ± 1.2	-12.0 ± 2.8
Hipparcos (Feast & Whitelock 1997)	14.8 ± 0.8	-12.0 ± 0.6
Cepheids (Dehnen & Binney 1998)	14.5 ± 1.5	-12.5 ± 2
Hipparcos proper motion (Mignard 2000):		
Early-type dwarfs	11.0 ± 1.0	-13.2 ± 0.5
Distant giants	14.5 ± 1.0	-11.5 ± 0.5
Stellar parallax (Olling & Dehnen 2003)	$\simeq 16$	$\simeq -17$

Table 2. Galactic constants (R_0, V_0).

Source	R_0 (kpc)	V_0 ($\mathrm{km\,s^{-1}}$)
Kerr and Lynden-Bell (1986)	8.2	220
Review before 1993 (Reid 1993)	8.0 ± 0.5	
Olling and Merrifield (1998)	7.1 ± 0.4	184 ± 8
VLBI Sgr A* (Ghez et al. 2008)	8.4 ± 0.4	
VLBI Sgr A* (Gillessen et al. 2009)	8.33 ± 0.35	
Maser astrometry (Reid et al. 2009)	8.4 ± 0.6	254 ± 16
Cepheids (Matsunaga et al. 2009)	8.24 ± 0.42	
VERA (Honma et al. 2012, 2015)	8.05 ± 0.45	238 ± 14

include Sofue and Rubin (2001) and Sofue (2013a), and the literature therein. Individual references are given in the related sections in this review.

2 Rotation of the Milky Way

2.1 Dynamical parameters representing the Galaxy

In this review, we use either the traditional Galactic constants of $(R_0, V_0) = (8.0\,\mathrm{kpc}, 200\,\mathrm{km\,s^{-1}})$, or the recently determined values, $(R_0, V_0) = (8.0\,\mathrm{kpc}, 238\,\mathrm{km\,s^{-1}})$ from observations using VERA (VLBI Experiment for Radio Astrometry) (Honma et al. 2012, 2015). Here, R_0 is the distance of the Sun from the Galactic Center and V_0 is the circular velocity of the local standard of rest (LSR) at the Sun (see Fich & Tremaine 1991 for review).

An approximate estimation of the mass inside the solar circle can be obtained for a set of parameters of $R_0 = 8$ kpc and $V_0 = 200$ to $238\,\mathrm{km\,s^{-1}}$, assuming spherical distribution of mass, as

$$M_0 = \frac{R_0 V_0^2}{G} = (7.44\,\text{to}\,1.05) \times 10^{10}\,M_\odot \sim 10^{11}\,M_\odot, \qquad (1)$$

with G being the gravitational constant, and the solar rotation velocity V_0 being related to R_0 as $V_0 = (A - B)R_0$, where A and B are the Oort's constants (Oort 1965), which are determined by measuring the radial velocity and proper motion of a nearby star. See Kerr and Lynden-Bell (1986) for a review regarding the Oort constants, and tables 1 and 2 for recent values.

Table 3. Dynamical parameters for the Galactic mass determination (Sofue 2013b).[*]

Subject	Component	No. of parameters
I. Axisymmetric structure (RC)	Black hole	(1) Mass
	Bulge(s)[†]	(2) Mass
		(3) Radius
		(4) Profile (function)
	Disk	(5) Mass
		(6) Radius
		(7) Profile (function)
	Dark halo	(8) Mass
		(9) Scale radius
		(10) Profile (function)
II. Non-axisymmetric structure (out of RC)	Bar(s)	(11) Mass
		(12) Maj. axis length
		(13) Min. axis length
		(14) z-axis length
		(15) Maj. axis profile
		(16) Min. axis profile
		(17) z-axis profile
		(18) Position angle
		(19) Pattern speed Ω_p
	Arms	(20) Density amplitude
		(21) Velocity amplitude
		(22) Pitch angle
		(23) Position angle
		(24) Pattern speed Ω_p
III. Radial flow (out of RC)	Rings	(25) Mass
		(26) Velocity
		(27) Radius

[*] In the present paper we review subject I.

[†] The bulge and bar may be multiple, increasing the number of parameters.

By the definition of rotation curve, we assume that the motion of gas and stars in the Galaxy is circular. This assumption puts significant limitation on the obtained results. In fact, the galactic motion is superposed by non-circular streams, such as a flow due to a bar, spiral arms, or expanding rings. The dynamical parameters of the Galaxy to be determined from observations, therefore, include those caused by both axisymmetric and non-axisymmetric structures. In table 3 we list the representative parameters and analysis methods (Sofue 2013b).

In the present paper, we review the methods to obtain parameters (1) to (10) in the table, which define the axisymmetric structure of the Galaxy as the first approximation to the fundamental galactic structure. Non-circular motions caused by a bar and spiral arms are beyond the scope of this review, and they are reviewed in the literature (e.g., Binney et al. 1991; Athanassoula 1992; Burton & Liszt 1993; Jenkins & Binney 1994).

2.2 Progress in the Galactic rotation curve

Figure 1 shows the progress in the determination of the rotation curve of the Milky Way Galaxy, and table 4 lists the major works in several decades. Before and until the 1970s, the inner rotation curve of the Milky Way has been extensively measured by the terminal-velocity method applied to radio line observations such as the H I line (Burton & Gordon 1978; Clemens 1985; Fich et al. 1989).

During the 1980s and 1990s, outer rotation velocities of stellar objects (OB stars) were measured by combining optical distances and CO-line velocities of associating molecular clouds (Blitz et al. 1982; Demers & Battinelli 2007). The H I thickness method was also useful for measuring the rotation of the entire disk (Merrifield 1992; Honma & Sofue 1997).

From 1990 and through the 2000s, VLBI (very long baseline interferometry) measurements of parallax and proper motions of maser sources and Mira variable stars provided advanced rotation velocities with high accuracy (Honma et al. 2007). It was also recently that the proper motions of a considerable number of stars were used for a rotation curve measurement (López-Corredoira 2014).

The most powerful tool to-date to measure the rotation of the Milky Way up to $R \sim 20$ kpc is the VERA, with which trigonometric determination of both 3D positions and velocities are done simultaneously for individual maser sources (Honma et al. 2007, 2012, 2015; Nakanishi et al. 2015; Sakai et al. 2015).

Since the 1990s, through studies of the kinematics of interstellar gas and infrared stars in the vicinity of the nucleus of our Galaxy, Sgr A*, the existence of a massive black hole has been revealed. The mass has been measured to be on $\sim 4 \times 10^6 \, M_\odot$ was measured by proper-motion measurements of infrared sources around the nucleus (Lindqvist et al. 1992; Genzel et al. 1994; Ghez et al. 1998; Gillessen et al. 2009).

For the total mass of the Galaxy including the extended dark halo, analyses of the outermost rotation curve and motions of satellite galaxies orbiting the Galaxy have been obtained in detail. The total mass of the Galaxy including the dark halo up to ~150 kpc has been estimated to be $\sim 3 \times 10^{11} \, M_\odot$ (Sofue 2015).

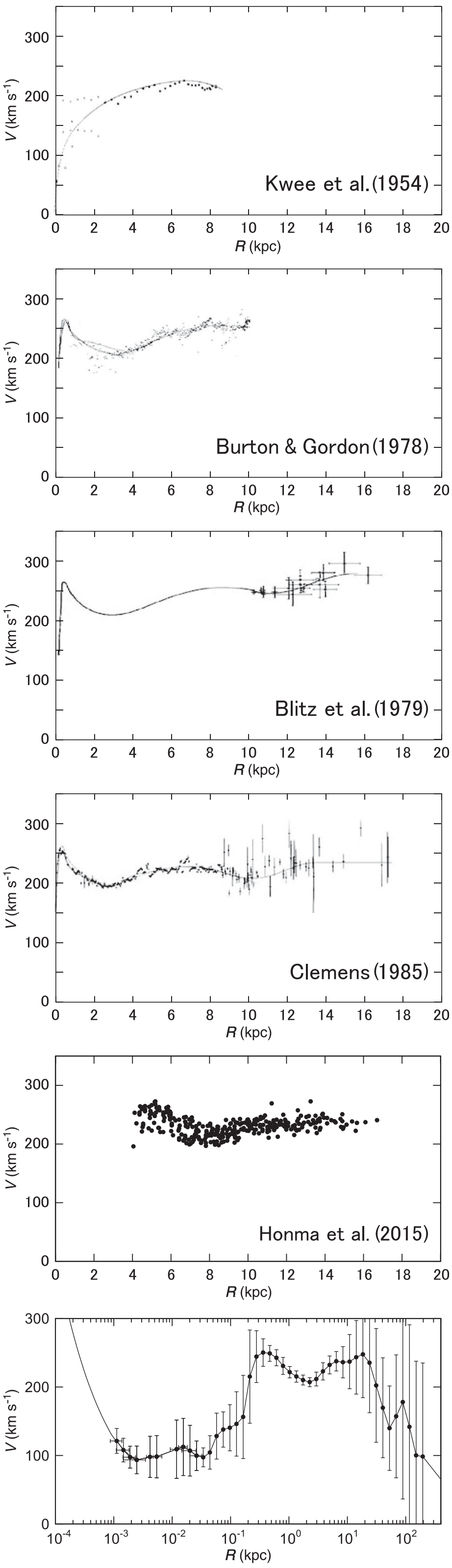

Fig. 1. Half a century of progress in rotation curve (RC) determination of the Milky Way. Top to bottom: 1950s (Kwee et al. 1954); 1970s—CO and H I (Burton & Gordon 1978; Blitz & Lada 1979); 1980s—composite of CO, H I, and optical (Clemens 1985); 2000s—most accurate trigonometric RC by maser sources with VERA (Honma et al. 2015); and a semi-logarithmic grand RC from the Galactic Center to half-way to M 31 (Sofue 2015).

Table 4. Rotation curves of the Milky Way Galaxy.

Source	Radii	Method	Remark*
Burton and Gordon (1978)	0–8 kpc	H I tangent	RC
Blitz and Lada (1979)	8–18 kpc	OB-CO association	RC
Clemens (1985)	0–18 kpc	CO	RC
Dehnen and Binney (1998)	8–20	Compil. + model	RC/Galactic constants
Genzel et al. (1997, 2000); Genzel, Eisenhauer, and Gillessen (2010); Genzel, Hollenbach, and Townes (1994); Ghez et al. (1998, 2008)	0–0.1 pc	IR spectroscopy	Orbits, V dispersion
Battinelli et al. (2013)	9–24 kpc	C stars	RC
Bhattacharjee et al. (2014)	0–200 kpc	Non-disk objects	RC/model fit
López-Corredoira (2014)	5–16 kpc	Red-clump giants μ	RC
Bobylev (2013); Bobylev and Bajkova (2015)	5–12 kpc	Masers/OB stars	RC/Galactic constants
Honma et al. (2012, 2015)	3–20 kpc	Masers, VLBI	RC/Galactic constants
Galazutdinov et al. (2015)	8–12 kpc	Ca II H,K line absorption	RC
Sofue et al. (2009); Sofue (2013b, 2015)	0–300 kpc	CO/H I/opt/compil.	RC/model fit

*RC = rotation curve.

2.3 Methods to determine the Galactic rotation curve

The radial velocity, v_r, and perpendicular velocity to the line of sight, v_p, of an object at a distance r orbiting around the Galactic Center are related to the circular orbital rotation velocity V as

$$v_r = \left(\frac{R_0}{R}V - V_0\right)\sin l, \tag{2}$$

and

$$v_p = \mu r = -\frac{s}{R}V - V_0\cos l, \tag{3}$$

where

$$s = r - R_0\cos l. \tag{4}$$

Here μ is the proper motion, and R is the galacto-centric distance, related to r and galactic longitude l by

$$R = \sqrt{r^2 + R_0^2 - 2rR_0\cos l}, \tag{5}$$

or

$$r = R_0\cos l \pm \sqrt{R^2 - R_0^2\sin^2 l}. \tag{6}$$

2.3.1 Terminal-velocity method inside the solar circle

Inside the solar circle, the Galactic disk has tangential points, at which the rotation velocity is parallel to the line of sight. Figure 2 shows the tangent velocities measured for the first quadrant of the Galactic disk (e.g., Burton & Gordon 1978).

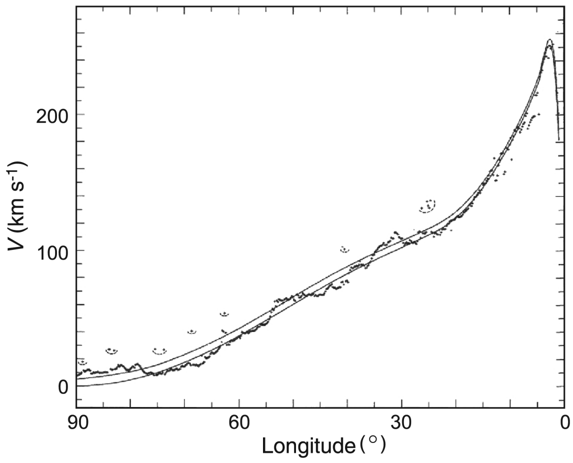

Fig. 2. CO and H I line tangent velocities for the inner rotation curve (Burton & Gordon 1978).

Maximum radial velocities $v_{r\,\mathrm{max}}$ (terminal or the tangent-point velocity) are measured by the edges of spectral profiles in the H I and CO line emissions at $0° < l < 90°$ and $270° < l < 360°$. The rotation velocity $V(R)$ is calculated using this velocity as

$$V(R) = v_{r\,\mathrm{max}} + V_0\sin l, \tag{7}$$

and the galacto-centric distance is given by

$$R = R_0\sin l. \tag{8}$$

2.3.2 Radial-velocity method

The method to calculate the rotation velocity using the radial velocity is applied to various objects, where

$$V(R) = \frac{R}{R_0}\left(\frac{v_r}{\sin l} + V_0\right). \tag{9}$$

In this method, the distance r has to be independently measured methods such as trigonometric and/or spectroscopic measurements. Often-used objects are OB stars or associations. The distances of OB stars are measured from their distance modulus, and the distance is assumed to be the same as that of its associated molecular cloud or H II region, the radial velocity of which is observed by molecular/recombination line measurements. However, errors in the photometric distances are usually large, resulting in large errors and in scatter of the outer rotation curve determinations.

2.3.3 Proper-motion method

The rotation velocity can also be measured by using proper motion μ as

$$V(R) = -\frac{R}{s}(v_\mathrm{p} + V_0 \cos l). \tag{10}$$

VLBI techniques have made it possible to employ this method, in equation (10) of which the distance r, proper motion v_p $(= r\mu)$, and radial velocity v_r are observed at the same time. Applying this technique to a number of maser sources, the outer rotation curve has been determined with high accuracy (Honma et al. 2012, 2015; Sakai et al. 2012, 2015; Nakanishi et al. 2015) (figure 1).

Proper motions of a large number of stars from Hipparcos observations combined with the 2MASS photometric data have recently been analyzed for galactic kinematics (Roeser et al. 2010; López-Corredoira 2014). Proper motions were obtained from the PPMXS catalogue from Hipparcos observations, and the distances were determined from K- and J-band photometry using the 2MASS star catalogue and correcting for the interstellar extinction. The red clump giant (RCG) stars were used for their assumed constant absolute magnitudes.

2.3.4 Trigonometric method using velocity vectors with VLBI

The ultimate method to investigate the Milky Way's rotation, without being bothered by various assumptions such as the circular rotation and/or a priori given solar constants, is the VLBI method, by which three-dimensional (3D) positions and motions of individual maser sources are measured simultaneously.

The VERA observations have most successfully obtained rotation velocities for several hundred Galactic maser sources within ∼10 kpc from the Sun. This project has introduced a new era in the Galactic astronomy, providing us with the most precise solar constants ever obtained (Honma et al. 2007, 2012, 2015; Nakanishi et al. 2015; Sakai et al. 2015).

When the three independent quantities of v_r, μ, and r are known or have been observed simultaneously, the 3D velocity vector can be determined uniquely without making any assumptions such as a circular orbit. The absolute value of the velocity vector is given by

$$V = \sqrt{U_\mathrm{p}^2 + U_\mathrm{r}^2}, \tag{11}$$

where

$$U_\mathrm{p} = v_\mathrm{p} + V_0 \cos l, \tag{12}$$

and

$$U_\mathrm{r} = v_\mathrm{r} + V_0 \sin l. \tag{13}$$

2.3.5 Ring thickness method

In the current methods, distances of individual objects are measured independently of radial velocities or proper motions. However, distances of diffuse and/or extended interstellar gases are not measurable. The H I-disk thickness method has been developed to avoid this inconvenience (Merrifield 1992; Honma & Sofue 1997), where annulus-averaged rotation velocities are determined in the entire disk. In the method, the angular thickness Δb of the H I disk is measured along an annulus ring of radius R, which is related to R and l by

$$\Delta b = \arctan\left(\frac{z_0}{R_0 \cos l + \sqrt{R^2 - R_0^2 \sin^2 l}}\right). \tag{14}$$

The longitudinal variation of Δb is uniquely related to the galacto-centric distance R, and is a function of $V(R)$. Since this method measures the averaged kinematics of the Galaxy, it represents a more global rotation curve than those based on the previously described methods.

2.4 Rotation in the Galactic Center

Because of its vicinity the Galactic Center rotation has been studied in more detail among the spiral galaxies, particularly in the nuclear region around Sgr A* which hosts the super-massive black hole.

Extensive CO-line observations of the Galactic Center have provided us with its high-quality and high-resolution longitude–velocity (LV) diagrams (e.g., Oka et al. 1998; Dame et al. 2001). Figure 3 shows the rotation curve in the central ∼100 pc as obtained by applying the terminal-velocity method to these LV diagrams (Sofue 2013b).

Further inside ∼0.1 pc of the Galactic Center, infrared proper-motion measurements of circumnuclear giant stars have shown that these stars are moving around Sgr A* in closed elliptical orbits. Analyses of the orbits showed high velocities that increase with the close vicinity of the nucleus, giving firm evidence for a massive black hole located at the same position as Sgr A* of ∼4 million solar masses (see sub-subsection 4.2.2).

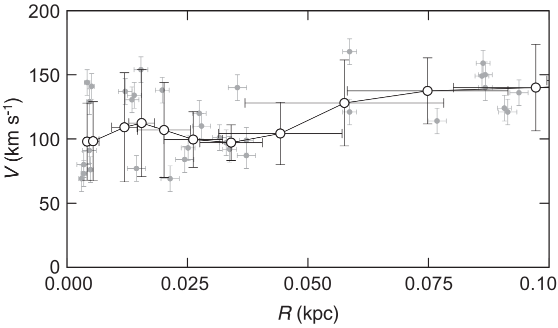

Fig. 3. Rotation velocities in the Galactic Center obtained by terminal-velocity method using position–velocity diagrams (gray dots, measured values; circles, running averaged values) (Sofue 2013b).

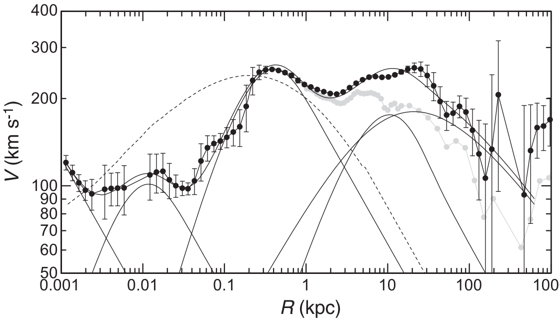

Fig. 4. Logarithmic rotation curve of the Galaxy for $V_0 = 238\,\mathrm{km\,s^{-1}}$ and deconvolution into a central black hole, two exponential-spherical bulges, an exponential flat disk, and a NFW (Navaro–Frenk–White) dark halo by the least-χ^2 fitting shown by thin lines. A classical de Vaucouleurs bulge shown by the dashed line is significantly displaced from the observation.

2.5 Logarithmic rotation curve: from black hole to dark halo

A rotation curve covering wider regions of the Galaxy has been obtained by compiling the existing data by rescaling the distances and velocities to the common Galactic constants $(R_0,\ V_0) = (8.0\,\mathrm{kpc},\ 200\,\mathrm{km\,s^{-1}})$ (Sofue et al. 2009). Rotation velocities in the outermost part of the Galaxy and beyond the disk were estimated by analyzing the radial velocities of globular clusters and satellite galaxies (Sofue 2013b).

Figure 4 shows a logarithmic rotation curve of the entire Milky Way. The enlarged scale toward the center is useful for analyzing the nuclear dynamics. The curve is drawn to connect the central rotation curve smoothly to the Keplerian motion representing the central massive black hole of mass $3.6 \times 10^6\,M_\odot$ (Ghez et al. 2005; Gillessen et al. 2009). The figure shows the continuous variation of the rotation velocity from the Galactic Center to the dark halo.

Detailed analyses of the rotation curve and deconvolution into mass components will be described in section 4.

2.6 Uncertainty and limitation of rotation curve analyses

2.6.1 Accuracy diagram

The accuracy of the obtained rotation curve of the Milky Way is determined not only by the measurement errors, but also by the employed methods and the location of the observed objects in the Galactic disk (Sofue 2011).

The most common method to calculate rotation velocity V using the radial velocity v_r and distance r yields

$$V_\mathrm{rot}^{v_\mathrm{r}} = \frac{R}{R_0}\left(\frac{v_\mathrm{r}}{\sin l} + V_0\right). \tag{15}$$

The error of the derived velocity is given by

$$\Delta V_\mathrm{rot}^{v_\mathrm{r}} = \sqrt{\delta V_{v_\mathrm{r}}^2 + \delta V_\mathrm{r}^2}, \tag{16}$$

where

$$\delta V_{v_\mathrm{r}}^2 = \frac{\partial V}{\partial v_\mathrm{r}}\delta v_\mathrm{r}, \quad \delta V_\mathrm{r} = \frac{\partial V}{\partial r}\delta r. \tag{17}$$

Remembering equations (5) and (9), we obtain

$$\Delta V_\mathrm{rot}^{v_\mathrm{r}} = \left[\left(\frac{R}{R_0 \sin l}\right)^2 \delta v_\mathrm{r}^2 + \left(\frac{s\ V}{R^2}\right)^2 \delta r^2\right]^{1/2}. \tag{18}$$

The rotation velocity using the proper motion v_p is given by

$$V_\mathrm{rot}^{\mu} = -\frac{R}{s}(v_\mathrm{p} + V_0 \cos l). \tag{19}$$

Knowing $R^2 - s^2 = R_0^2 \sin^2 l$, we have the errors in this quantity as

$$\Delta V_\mathrm{rot}^{\mu} = \frac{R}{s}\left[\delta v_\mathrm{p}^2 + \left(\frac{R_0^2 v_\mathrm{p} \sin^2 l}{s\,R^2}\right)^2 \delta r^2\right]^{1/2}. \tag{20}$$

In figure 5a we present examples of the accuracy diagram of the radial-velocity method for a set of measurement errors, $\delta v_\mathrm{r} = 1\,\mathrm{km\,s^{-1}}$ and $\delta r/r = 0.02$, or 2%. It is readily seen that the accuracy is highest along the tangent point circle (white regions), proving that the tangent-point circle is a special region for accurate rotation curve determination. In contrast, the largest error is yielded near the singularity line running across the Sun and the Galactic Center (GC), where the circular rotation is perpendicular to the line-of-sight.

In figure 5b we show an accuracy diagram of the proper-motion method for $\delta v_\mathrm{p}/r = 1\,\mathrm{km\,s^{-1}\,kpc^{-1}}$, or $\delta\mu = 0.21\,\mathrm{mas\,yr^{-1}}$, and $\delta r/r = 0.02$. Contrary to the radial-velocity method, the error becomes smallest along the Sun–GC line, but it is largest near the tangent point circle, where equation (20) diverges. Thus, the tangent-point circle is

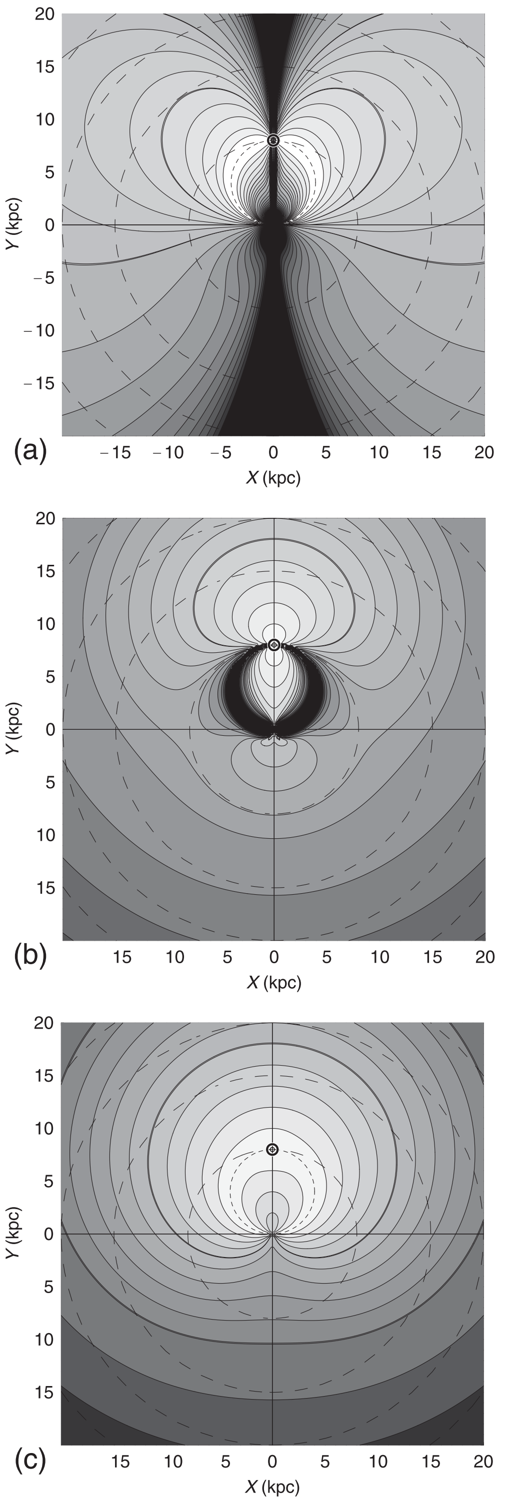

Fig. 5. (a) Accuracy diagrams $\Delta V_{\rm rot}^{v_{\rm r}}(X, Y)$ for $\delta v_{\rm r} = 1\,{\rm km\,s^{-1}}$ and $\delta r/r = 0.02$ (2% distance error), (b) $\Delta V_{\rm rot}^{\mu}(X, Y)$ for $\delta\mu = 0.2\,{\rm mas\,yr^{-1}}$, and (c) $\Delta V_{\rm rot}^{\rm vec}(X, Y)$ for $\delta v_{\rm p}/r = 1\,{\rm km\,s^{-1}\,kpc^{-1}}$ corresponding to $\delta\mu = 0.21\,{\rm mas\,yr^{-1}}$, $\delta v_{\rm r} = 1\,{\rm km\,s^{-1}}$, and $\delta r/r = 0.02$ (Sofue 2011).

a singular region in this method. This behavior is completely opposite to that seen in the case for the radial-velocity method, and the radial-velocity and the proper-motion methods are complementary to each other.

Figure 5c shows the same, but for errors in velocity vector method using the 3D trigonometric measurement. This method yields much milder error variations in the entire Galaxy, showing no singular regions.

2.6.2 Implication

The accuracy diagram, $\Delta V_{\rm rot}^{v_{\rm r}}(X, Y)$, demonstrates the reason why the rotation curve is nicely determined along the tangent-point circle, which is a special region yielding the highest accuracy determination of rotation velocity. The diagram also suggests that the "butterfly" areas at $l \sim 100^\circ$–135° and $l \sim 225^\circ$–280° are suitable regions for outer rotation curve work using the radial-velocity method.

In the proper-motion method, the most accurate measurement is obtained along the Sun–Galactic Center line, as indeed realized by Honma et al. (2007). It must also be emphasized that the minimum error area is widely spread over $l \sim 120^\circ$–250° in the anti-center region, as well as in the central region inside the tangent-point circle. On the other hand, the largest error occurs along the tangent-point circle, which is the singularity region in this method.

2.7 Radial-velocity and proper-motion fields

If the rotation curve is determined, we are able to measure kinematical distances of any objects in the Galactic disk by applying the velocity-space transformation, assuming the circular rotation of the objects (Oort et al. 1958; Nakanishi & Sofue 2003, 2006, 2016). The kinematical distance is obtained either from radial velocity or from proper motion using equations (2) and (3), and the velocities can be represented as a map on the galactic plane, as shown in figure 6.

It may be worth mentioning that the solar circle is a special ring, where the radial velocity is zero, $v_{\rm r} = 0$, whereas the proper motion μ has a constant value, with

$$\mu_\odot = -\frac{V_0}{R_0} = \Omega_0, \tag{21}$$

which yields $\mu_\odot = -5.26\,{\rm mas\,yr^{-1}}$ for $R_0 = 8\,{\rm kpc}$ and $V_0 = 200\,{\rm km\,s^{-1}}$.

VLBI trigonometric measurements have made it possible to apply this method to determine kinematical distance r_μ. However, the radial-velocity field is currently used more commonly to map the distributions of stars and interstellar gas in the galactic plane because of its convenience.

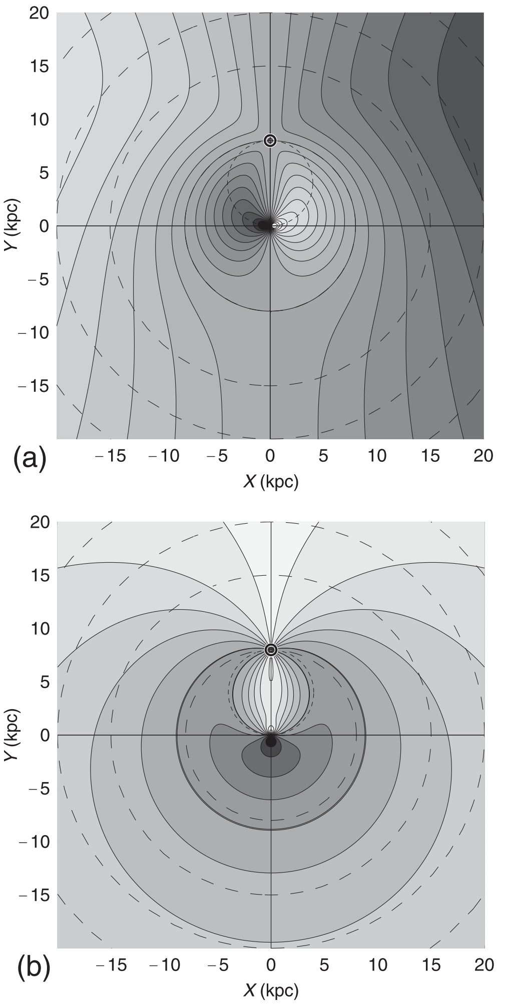

Fig. 6. (a) Radial-velocity field $v_r(X, Y)$ with contour increment 20 km s^{-1}, and (b) proper-motion field $\mu(X, Y)$ with contour increment 1 mas yr^{-1}. The circle near the solar orbit is for 5 mas yr^{-1}.

2.8 Velocity-to-space transformation

If a rotation curve $V(R)$ is obtained or assumed, the radial velocity v_r of an object in the galactic disk is uniquely calculated by equation (2). Figure 6 shows a thus-calculated distribution of the radial velocity, or the velocity field. Equation (2) includes the distance and longitude. Therefore, the equation can be solved inversely to determine the position of an object using its radial velocity. This procedure is called the velocity-to-space (VTS) transformation.

By this method, the position of an object outside the solar circle is uniquely determined, but it has two-fold solutions for objects inside the solar circle. In order to solve this two-folding distance problem, further information such as the apparent sizes of individual clouds and/or disk thickness is employed.

Applying the VTS transformation, galactic maps of H I and H_2 gases are obtained as follows. Column densities of H I and H_2 gases are related to the H I and CO line intensities as

$$N_{\rm H\,I}[{\rm H\,cm^{-2}}] = C_{\rm H\,I} \int T_{\rm H\,I}(v) dv [{\rm K\,km\,s^{-1}}], \tag{22}$$

and

$$N_{\rm H_2}[{\rm H_2\,cm^{-2}}] = C_{\rm H_2} \int T_{\rm CO}(v) dv [{\rm K\,km\,s^{-1}}], \tag{23}$$

where $T_{\rm H\,I}$ and $T_{\rm CO}$ are the H I and CO line brightness temperatures, and C_i are the conversion factors; $C_{\rm H\,I} = 1.82 \times 10^{18}$ [H cm^{-2}] and $C_{\rm H_2} \sim 2 \times 10^{20} f(R, Z)$ [$\rm H_2$ cm^{-2}], with f a correction factor depending on R (e.g., Arimoto et al. 1996).

The volume density of the gas corresponding to radial velocity v_r is obtained by

$$n_{\rm H\,I} = \frac{dN_{\rm H\,I}}{dr} = \frac{dN_{\rm H\,I}}{dv_{\rm r}} \frac{dv_{\rm r}}{dr} = C_{\rm H\,I} T_{\rm H\,I}(v_{\rm r}) \frac{dv_{\rm r}}{dr}, \tag{24}$$

and

$$n_{\rm H_2} = \frac{dN_{\rm H_2}}{dr} = \frac{dN_{\rm H_2}}{dv_{\rm r}} \frac{dv_{\rm r}}{dr} = C_{\rm H_2} T_{\rm CO}(v_{\rm r}) \frac{dv_{\rm r}}{dr}. \tag{25}$$

These formulae enable us to create a face-on view of the interstellar medium (ISM) in the Galaxy, where the 3D distribution of the volume densities of the H I and H_2 gases can be mapped. Figure 7 shows the thus-obtained face-on view of the Galactic disk (Nakanishi & Sofue 2003, 2006, 2016).

3 Rotation curves of spiral galaxies

3.1 Progress in rotation curve studies evidencing for the dark halo

The rotation of galaxies was discovered a century ago when inclined spectra were observed across the nuclei of nearby galaxies. The modern era of rotation curves started in the 1950s, when red-sensitive photographic plates were used to observe the Hα λ6563 and [N II] λ6584 emission lines arising from H II regions. A history review of the developments in galaxy rotation has been given in Sofue and Rubin (2001).

Since the early measurements, flat rotation curves were routinely observed in spiral galaxies. Figure 8 shows a progress in the rotation curve obtained for the spiral galaxy M 31. Late in the last century, larger and more advanced telescopes and detectors in optical, infrared, and radio observations, combined with higher spectral resolution, have allowed us to obtain higher accuracy rotation curves at farther distances. The generally observed "flat rotation" in disk galaxies has shown the existence of massive dark halos around galaxies.

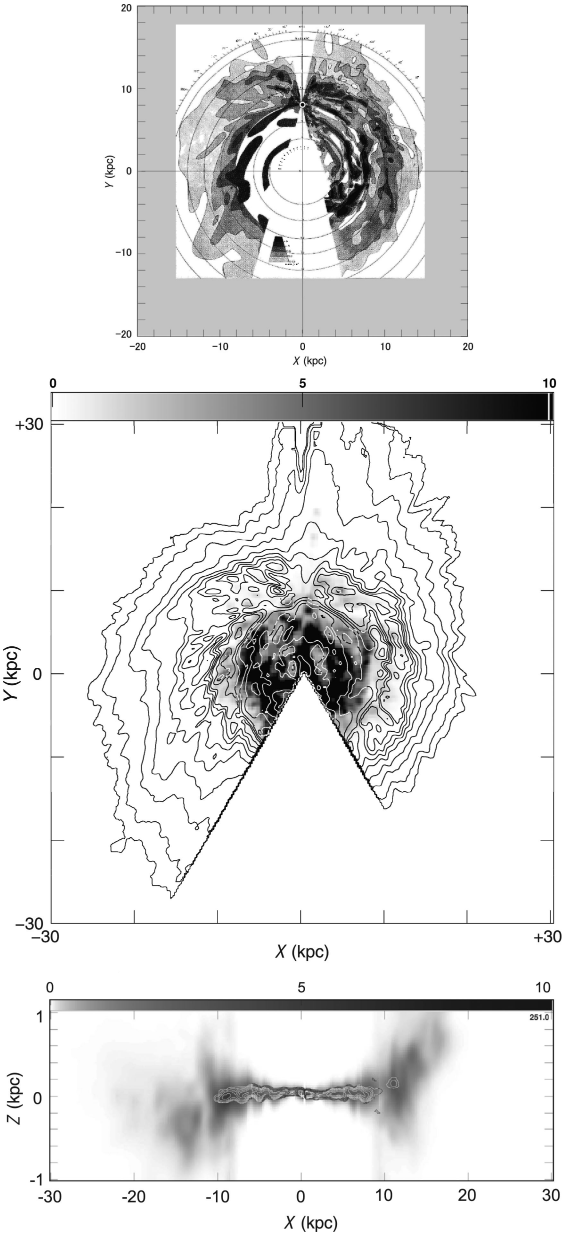

Fig. 7. (Top) 2D H I map of the Galaxy, showing the distribution of volume density of the H I gas in the galactic plane on the assumption of circular rotation of the disk (Oort et al. 1958). (Middle) Surface densities of H I (contours) and H_2 (gray-scale) gases obtained by integrating the 3D maps in the *Z*-direction (Nakanishi & Sofue 2016). (Bottom) H I and H_2 cross-section map of the Galaxy in the (*X*, *Z*) plane across the Galactic Center. Shown here are the volume densities H I (extended thick disk in gray-scale) and H_2 (thin disk by contours) (Sofue & Nakanishi 2016). Note that the *Z*-axis is enlarged by 4 times.

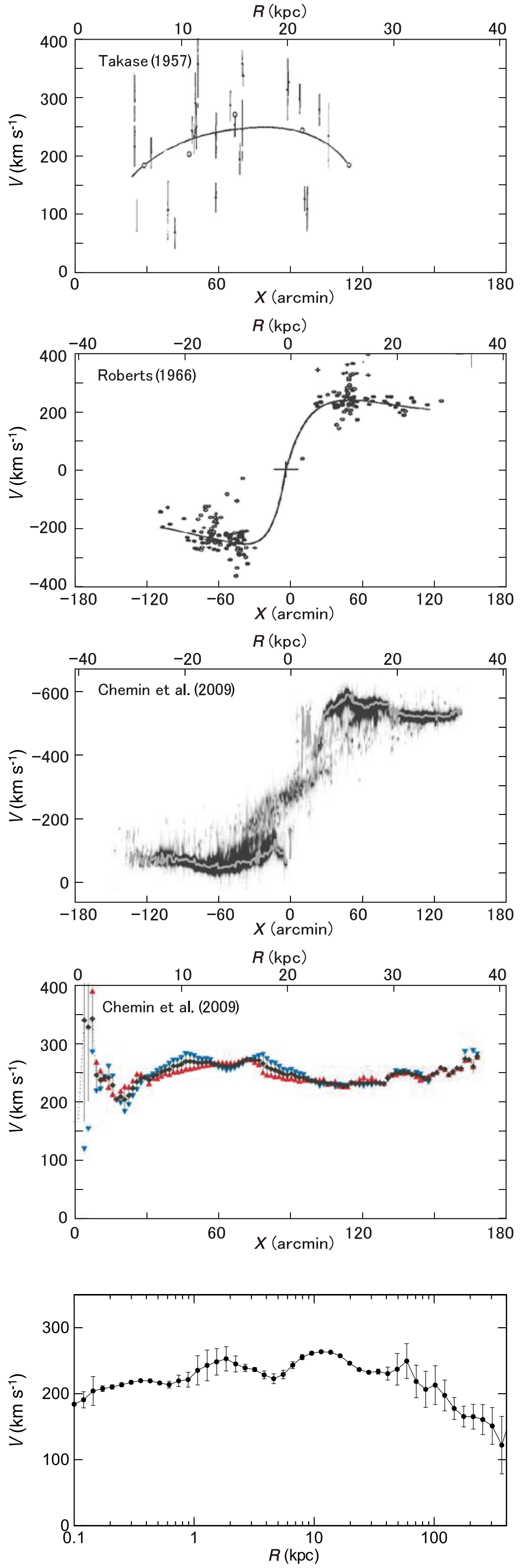

Fig. 8. Half a century of progress in the rotation curve of M 31. From top to bottom: 1950s—a rotation curve using data obtained by M.U. Mayall et al. in the 1940s (Takase 1957); 1960s—rotation curve in the H I 21 cm line (Roberts 1966); a modern position–velocity diagram and a rotation curve in H I, showing flat rotation up to 40 kpc (Chemin et al. 2009); and a grand rotation curve from the center to ∼300 kpc in semi-logarithmic scaling (Sofue 2013b). (Color online)

3.2 Observations of rotation velocities

In this subsection we review the progress in obtaining rotation curves and related techniques and analysis methods. The content is based on our earlier review in Sofue and Rubin (2001), with recent topics and particular progress

Table 5. Large catalogues of rotation curves in the two decades.

Source*	Objects	Distances	Method†	Catalogue type†
Mathewson, Ford, and Buchhorn (1992)	965 southern spirals	$\lesssim$100 Mpc	Hα/H I	RC/TF
Amram et al. (1994)	21 NGC/UGC	Cluster	Hα	RC/VF/table
Universal RC (since 1995)	967 southern spirals	Nearby	Avg. of comp.	Universal RC
Makarov et al. (1997, 2001)	135 edge-on	$\sim$100 Mpc	Hα	RC
Vogt et al. (2004a, 2004b)	329 spirals	$z < 0.045$	Hα/H I, RC, M/L, FuP	
Fridman et al. (2005)	15 Sb/Sc/NGC	10–70 Mpc	Hα/FP	RC/PV/VF
GHASP (since 2002)	85 spirals		Hα/FP	RC/VF
Márquez et al. (2002)	111 spipral/NGC		Hα/H II	RC
Blais-Ouellette et al. (2004)	6 Sb/Sc	$\lesssim$20 Mpc	FP	RC/VF
Big FP Hα Survey (since 2005)	21 barred spirals	2–38 Mpc	Hα FP	RC, VF
Noordermeer et al. (2005, 2007)	19 S0/Sa/U,NGC	15–65 Mpc	Hα/H I	RC/PV/VF
THINGS (2008)	19 Nearby NGC	Nearby	H I	RC/PV/VF
Spano et al. (2008)	36 NGC	Nearby	H I	RC
DiskMass (2010–2013)	146 face-on	$B < 14.7$	Hα/[O III]/Ca II/IS	RC/VF
Nearby Galaxies RC (since 1996)	$\sim$100 Sb/Sc/NGC	Nearby+Virgo	Hα/CO/H I	RC/PV
McGaugh, Rubin, and de Blok (2001)	36 LSB		Hα/slit	RC
de Blok and Bosma (2002)	26 LSB/UGC	3–45 Mpc	Hα/H I	RC/PV
Swaters et al. (2009)	62 LSB dw/Ir/UGC	Nearby	Hα	RC/PV

** Universal RC*: Persic and Salucci (1995), Persic, Salucci, and Stel (1996), Salucci et al. (2007); *GHASP*: Garrido et al. (2002, 2004, 2005); *Big FP Hα Survey*: Hernandez et al. (2005), Daigle et al. (2006), Dicaire et al. (2008); *THINGS*: de Blok et al. (2008); *DiskMass*: Bershady et al. (2010a, 2010b), Martinsson et al. (2013a, 2013b); *Nearby Galaxies RC*: Sofue (1996, 1999, 2016), Sofue et al. (2003).

†RC = rotation curve, TF = Tully–Fisher relation, VF = velocity field, PV = position–velocity diagram, FP = Fabry Perot, FuP = fundamental plane, IS = integral fiber spectroscopy.

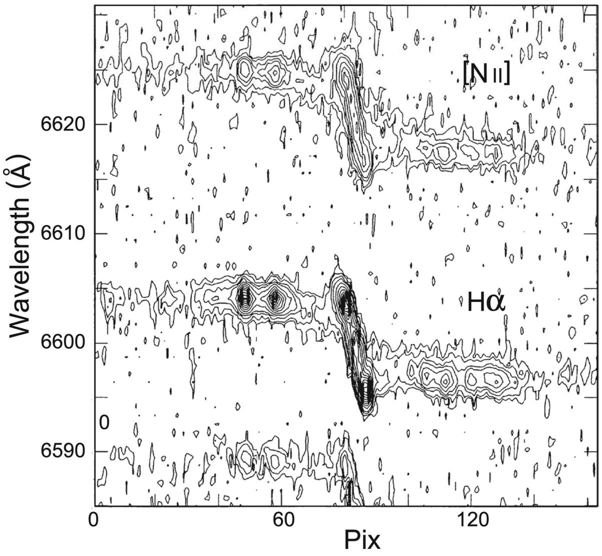

Fig. 9. Slit spectrum of the Hα 6563 Å and [N II] 6584 Å lines along the major axis of Sb galaxy NGC 4527 (Sofue et al. 1999).

added in. In table 5 we list the major papers in which rotation curve data are available in machine-readable formats, or in figures and tables.

3.2.1 Optical observations

Observations of optical emission lines such as Hα and [N II] lines sample population I objects, particularly H II regions associated with star-forming regions in the galactic disk (figure 9). These objects have small velocity dispersion compared to the rotation velocity, which allows us to derive circular velocities without suffering from relatively high velocity components from population II stars. The traditional method to derive rotation curves is long slit spectral observation along the major axis of disk galaxies (Rubin et al. 1982a, 1982b, 1985; Corradi et al. 1991; Mathewson et al. 1992; Amram et al. 1994; Courteau 1997; Sofue et al. 1998).

On the other hand, absorption lines, showing high velocity dispersion and slower rotation, manifest kinematics of population II stars composed of spheroidal components and thick disks. Their line width is used to estimate the virial mass through the pressure term in the equation of motion. In this paper, however, we concentrate on the low velocity dispersion component for rotation velocities.

3.2.2 Two-dimensional spectroscopy for velocity fields

Fabry–Perot spectrographs are used to measure two-dimensional velocity fields in disk galaxies. Velocity fields include information not only on the global galactic rotation, but also on non-circular stream motions due to spiral arms and bars (Vaughan 1989; Vogel et al. 1993; Regan & Vogel 1994; Weiner & Williams 1996; Garrido et al. 2002, 2004; Kamphuis & Briggs 1992; Hernandez et al. 2005; Daigle et al. 2006; Shetty et al. 2007; Dicaire et al. 2008).

The recent "DiskMass" survey of disk galaxies observed the largest sample of nearly face-on galaxies brighter than $B = 14.7$ with a disk size of 10″ to 20″ from the Upsala Galaxies Catalogue (UGC), and obtained their two-dimensional (2D) dynamical data (Bershady et al. 2010a, 2010b; Martinsson et al. 2013a, 2013b; Westfall et al. 2014). They employed integral-field spectroscopy fiber instruments to measure stellar and ionized gas kinematics, covering [O III]λ5007 and Hα lines. They also observed the Mg Ib and Ca II near-infrared triplet in stellar absorption to study the kinematics of spheroidal and old disk components.

3.2.3 Infrared spectroscopy

Spectral observations in the infrared wavelengths, including the Pα and/or [Si VI] lines, and the integral field analysis technique are powerful tools to reveal the kinematics of dusty disks (Krabbe et al. 1997; Tecza et al. 2001). They are particularly useful in the nuclear regions of spiral galaxies, where dust extinction is so significant that even such a red line as Hα is heavily obscured. Infrared observations are also powerful for mergers with dust-buried nuclei.

The rotation of the outer disks of galaxies is crucial in deriving the mass in the dark halo, while observations are still scarce because of the faintness and a small number of emission regions. Not only bright H II regions but also planetary nebulae and satellite galaxies are used as test particles for determining the mass distribution in outer regions.

3.2.4 H I and CO lines

The 21 cm H I line is powerful in obtaining kinematics of an entire spiral galaxy, because the radial extent in H I gas is usually much greater than that of the visible disk. H I measurements have played a fundamental role in establishing the flatness of rotation curves in spiral galaxies (e.g., Bosma 1981a, 1981b).

The CO molecular lines in the millimeter wave range are valuable in studying the kinematics of the inner disk and central regions of spiral galaxies because of their higher concentration toward the center than H I, which is deficient in the center, and for their extinction free nature against the central dusty disks (Sofue 1996, 1997).

3.3 Methods to determine rotation velocities

The rotation curve of a galaxy is defined as the trace of the terminal velocity on the major axis corrected for the inclination of the galaxy's disk. The observed lines are integration of various velocity components along the line of sight through the galaxy disk. Hence, the intensity peaks do not necessarily represent the terminal velocities.

3.3.1 Peak-intensity and intensity-weighted velocities

The velocity at which the line intensity attains its maximum, which is called the peak-intensity velocity, is often adopted to represent the rotation velocity (Mathewson et al. 1992; Mathewson & Ford 1996). A more popular method is to measure the intensity-weighted velocity which is sometimes approximated by a centroid velocity of the half-maximum values of a line profile (Rubin et al. 1982a, 1985). The intensity-weighted velocity is defined by

$$V_{\rm int} = \frac{\int I(v_{\rm r}) v_{\rm r} dv_{\rm r}}{\int I(v_{\rm r}) dv_{\rm r}}. \tag{26}$$

Here, $I(v_{\rm r})$ is the intensity as a function of the radial velocity. Rotation velocity is then given by

$$V_{\rm rot} = (V_{\rm int} - V_{\rm sys})/\sin i, \tag{27}$$

where i is the inclination angle between the galactic rotation axis and the line-of-sight and $V_{\rm sys}$ is the systemic velocity of the galaxy.

However, the intensity-weighted velocity always gives an underestimated rotation velocity because of the finite resolution of observation, due to which the plus and minus velocities in both sides of the nucleus are not resolved but are averaged. Thus, derived rotation curves often start from zero velocity at the center. However, the nucleus is the place that is hosting a massive black hole and a high-density bulge core, where gas and stars are moving most violently. Therefore, one must apply the peak-intensity velocity and/or intensity-weighted velocity methods carefully, because these methods often largely underestimate the central rotation velocities. However, they usually result in good approximations in sufficiently resolved outer disks.

3.3.2 Terminal-velocity and envelope-tracing method

The terminal velocity $V_{\rm t}$ in a position–velocity (PV) diagram is defined by the velocity at which the intensity becomes equal to

$$I_{\rm t} = [(\eta I_{\rm max})^2 + I_{\rm lc}^2]^{1/2}, \tag{28}$$

where $I_{\rm max}$ is the maximum intensity and $I_{\rm lc}$ is the intensity representing the lowest contour, which is often taken at ∼3 rms noise level in the PV diagram. The fraction η(0.2–0.5) represents the critical intensity level of the line profile.

The rotation velocity is then derived as

$$V_{\rm rot} = (V_{\rm t} - V_{\rm sys})/\sin i - (\sigma_{\rm ISM}^2 + \sigma_{\rm obs}^2)^{1/2}, \tag{29}$$

where $\sigma_{\rm ISM}$ and $\sigma_{\rm obs}$ are the velocity dispersion of the interstellar gas and the velocity resolution of observations, respectively. The interstellar velocity dispersion is of the

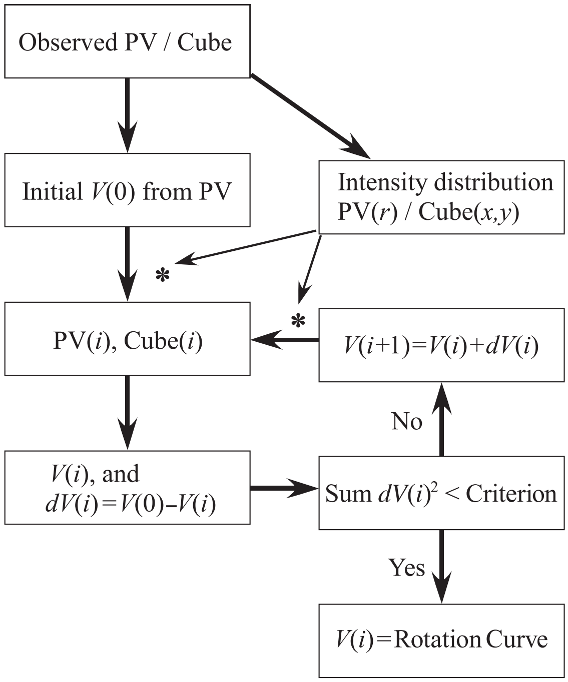

Fig. 10. Iteration method of rotation curve fitting using PV diagrams and/or 3D cube.

order of $\sigma_{\rm ISM} \sim 7$ to $10\,{\rm km\,s^{-1}}$, while $\sigma_{\rm obs}$ depends on the instruments used.

3.3.3 Iteration methods using a PV diagram and a 3D cube

A reliable method to estimate the rotation velocity is the iteration method, with which the rotation curve is iteratively adjusted until the observed PV diagram is reproduced by the calculated PV diagram using the rotation curve (Takamiya & Sofue 2002). In this method, an initial rotation curve RC_0 is settled from the observed PV diagram (PV_0) using any method given above. Using RC_0 and the observed radial distribution of the intensity, a PV diagram, PV_1, is constructed. The difference between PV_1 and PV_0 is then used to correct RC_0 to obtain a corrected rotation curve, RC_1. This RC_1 is used to calculate another PV diagram, PV_2, using the observed intensity distribution, from which the next iterated rotation curve, RC_2, is obtained by correcting for the difference between PV_2 and PV_0. This procedure is iteratively repeated until PV_i and PV_0 become identical within the error, and the final PV_i gives the most reliable rotation curve. Figures 10 and 11 illustrate the method.

3.3.4 3D cube iteration

The PV diagram along the major axis represents only one-dimensional (1D) velocity information along the major axis. The next-generation measurement of rotation velocities would be to utilize a 3D spectral data cube of the entire galaxy. This will be particularly useful for optically thin radio lines in the central regions, such as H I and CO lines. The reduction procedure would be similar to that for the PV iteration method. We first settle an approximate rotation curve, and calculate a data cube using this rotation curve and observed intensity distribution. The calculated cube is then compared with the original cube, and the difference is used to correct for the initially assumed rotation curve. This procedure is repeated iteratively to minimize the difference between the calculated and observed cubes. In the 3D iteration method, the entire data cube is analyzed without losing information, and we would be able to reach an ultimate rotation curve of a galaxy. This method is particularly useful for obtaining a rotation curve in the central region, where observational resolution is not sufficient.

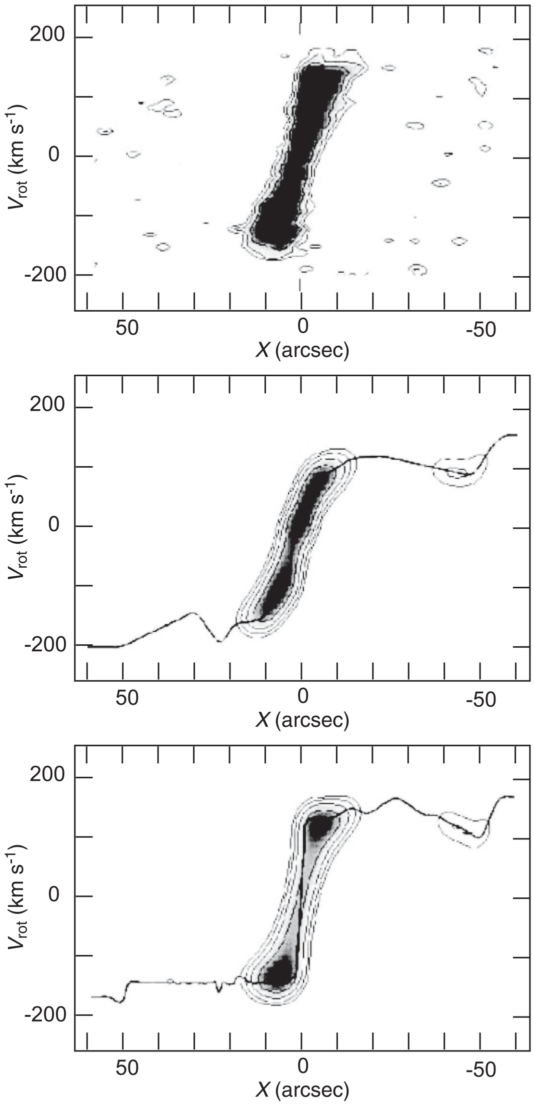

Fig. 11. Iteration method: PV diagram of NGC 4536 in the CO line (top); an approximate rotation curve using the peak-intensity method and corresponding PV diagram (middle); the final rotation curve and reproduced PV diagram (bottom).

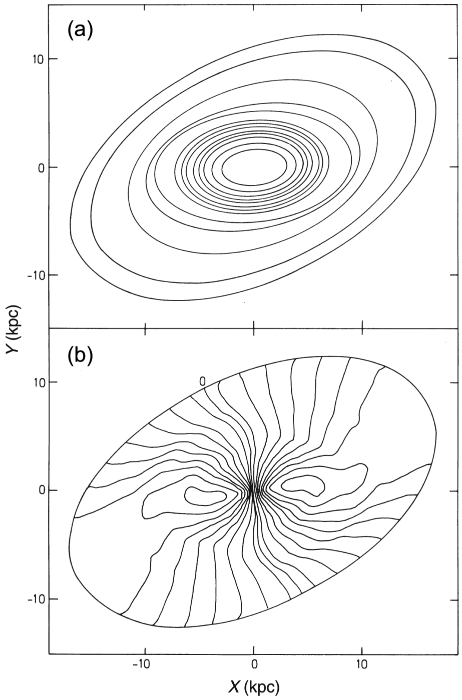

Fig. 12. Tilted rings and velocity field fitted to H I velocity fields of NGC 5055 (Bosma 1981b).

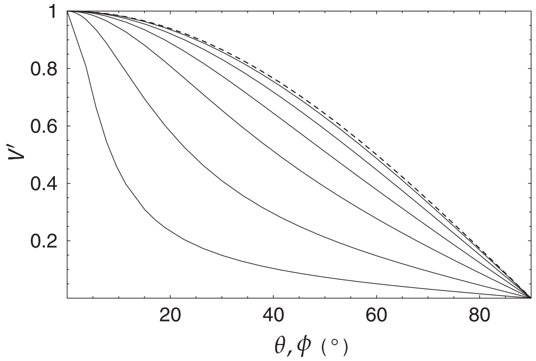

Fig. 13. Variation of $V' = v_{\rm r}/v_{\rm r,\,max}$ along a tilted-ring as a function of position angle ϕ (solid line) for different inclinations (from bottom, lines are $i = 85^\circ$, 75°, 60°, 45°, 30°, and 15°). Variation against azimuthal angle θ is shown by the dashed line.

3.3.5 Tilted-ring method for rotation velocity

The rotation velocity $V_{\rm rot}$, inclination angle i, and observed radial velocity $v_{\rm r}$ relative to the systemic velocity are related to each other as

$$v_{\rm r}(r, \theta) = V_{\rm rot}(r) \cos\theta \sin i, \tag{30}$$

where θ is the azimuthal angle in the disk of a measured point from the major axis. Obviously the rotation velocity and inclination are coupled to yield the same value of $v_{\rm r}$.

The most convenient way to derive a rotation curve is to measure radial velocities along the major axis using PV diagrams. Thereby, the inclination angle i has to be measured independently, or assumed. Given the inclination, the rotation velocity is obtained by

$$V_{\rm rot} = \frac{v_{\rm r}}{\sin i}, \tag{31}$$

with $v_{\rm r} = v_{\rm r}(r, 0)$.

Inclination angle i is measured from the major-to-minor axial length ratio of optical isophotes of a galaxy. An alternative way is to compare the integrated H I line width with that expected from the Tully–Fisher relation (Shetty et al. 2007). However, as equation (31) shows, the error in the resulting velocity is large for small i, and the result diverges for a face-on galaxy.

If a velocity field is observed, coupling of the rotation velocity and inclination can be solved using the tilted-ring technique to determine either the rotation velocity or the inclination (figure 12; Bosma 1981a, 1981b; Begeman 1989; Józsa et al. 2007). The radial velocity $v_{\rm r}$ is related to position angle ϕ and azimuthal angle θ as

$$f(\theta, i) = \frac{v_{\rm r}}{v_{\rm r,max}} = \cos\theta(\phi, i), \tag{32}$$

with

$$\theta(\phi, i) = \arctan\left(\frac{\tan\phi}{\cos i}\right), \tag{33}$$

and $v_{\rm r,\,max}$ is the maximum value along an annulus ring.

Figure 13 shows variations of $\cos\theta(\phi)$, or $v_{\rm r}$ normalized by its maximum value along an annulus ring, as functions of ϕ and θ for different values of inclination. The functional shape against ϕ is uniquely dependent on inclination i, which makes it possible to determine the inclination angle by iterative fitting of $v_{\rm r}$ with the function. Once i is determined, $V_{\rm rot}$ is calculated using $v_{\rm r}$. Thus, both i and $V_{\rm rot}$ are obtained simultaneously.

In an often-adopted method, the galactic disk is divided into many oval rings, whose major axis' position angles are determined by tracing the maximum saddle loci of the velocity field. Along each ring the angle θ is measured from the major axis. Observed values of $f(\theta, i)$ are compared with calculated values, and the value of i is adjusted until χ^2 gets minimized. The value of i yielding the least χ^2 is adopted as the inclination of this ring. This procedure is applied to neighboring rings iteratively, to yield the least χ^2 over all the rings. Begeman (1989) has extensively studied the tilted-ring method, and concluded that it is not possible to determine inclinations for galaxies whose inclination angles are less than 40°. Recently, more sophisticated methods incorporating the velocity field as a 3D data cube (velocity, x, and y) have been developed in order to fit

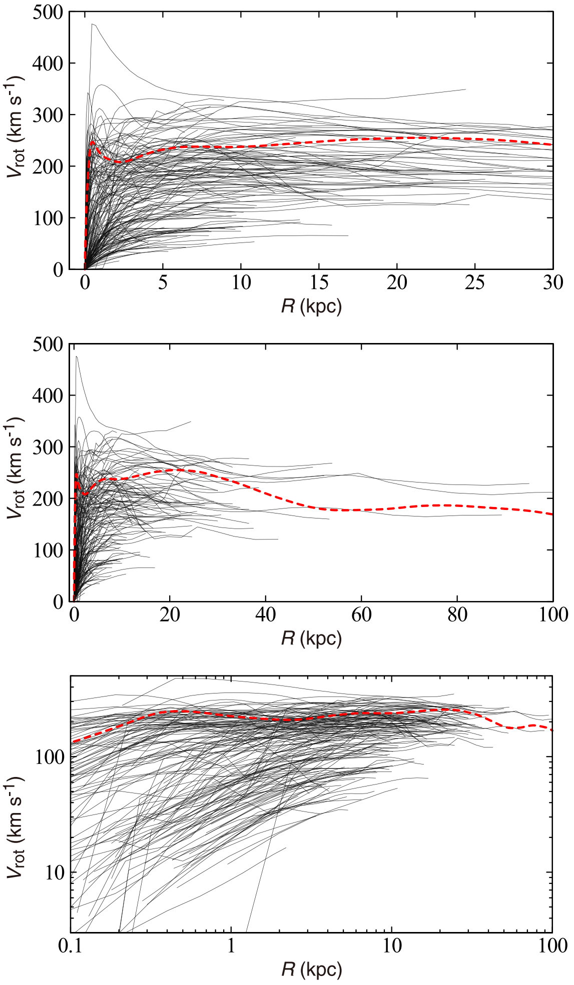

Fig. 14. Rotation curve compilation (Sofue 2016), which includes those from Whitmore, McElroy, and Schweizer (1987), Olling (1996), Sofue (1996), Ryder et al. (1998), Sofue et al. (1999, 2003), Márquez et al. (2004), Garrido et al. (2005), Gentile et al. (2007, 2015), Noordermeer et al. (2007), de Blok et al. (2008), Scarano et al. (2008), Swaters et al. (2009), Bershady et al. (2010a, 2010b), Hlavacek-Larrondo et al. (2011a, 2011b), Erroz-Ferrer et al. (2012), Martinsson et al. (2013a), and Richards et al. (2015). (Color online)

disk rotation curves (Bouché et al. 2015; Di Teodoro & Fraternali 2015).

3.3.6 Tilted-ring method for inclination

The tilted-ring method is useful for determining the velocity for highly and mildly inclined galaxies, but it fails when the galaxy is nearly face-on (figure 13). This property, in turn, may be used to determine the inclination by assuming the rotation velocity, remembering that the inclination is written as $\sin i = v_{\rm r}/V_{\rm rot}$, which means that the inclination can be determined by measuring $v_{\rm r}$, if $V_{\rm rot}$ is given.

This equation is used for the determination of inclination using the Tully–Fisher relation: the intrinsic line width is determined by the disk luminosity and is compared with the observed line width to estimate the inclination angle. The equation can be used to determine inclinations of individual annulus rings, if the rotation curve is given. This principle has been applied to analyzing the warping of the outer H I disk of the face-on galaxy NGC 628 (Kamphuis & Briggs 1992) and of M 51 (figure 20; Oikawa & Sofue 2014).

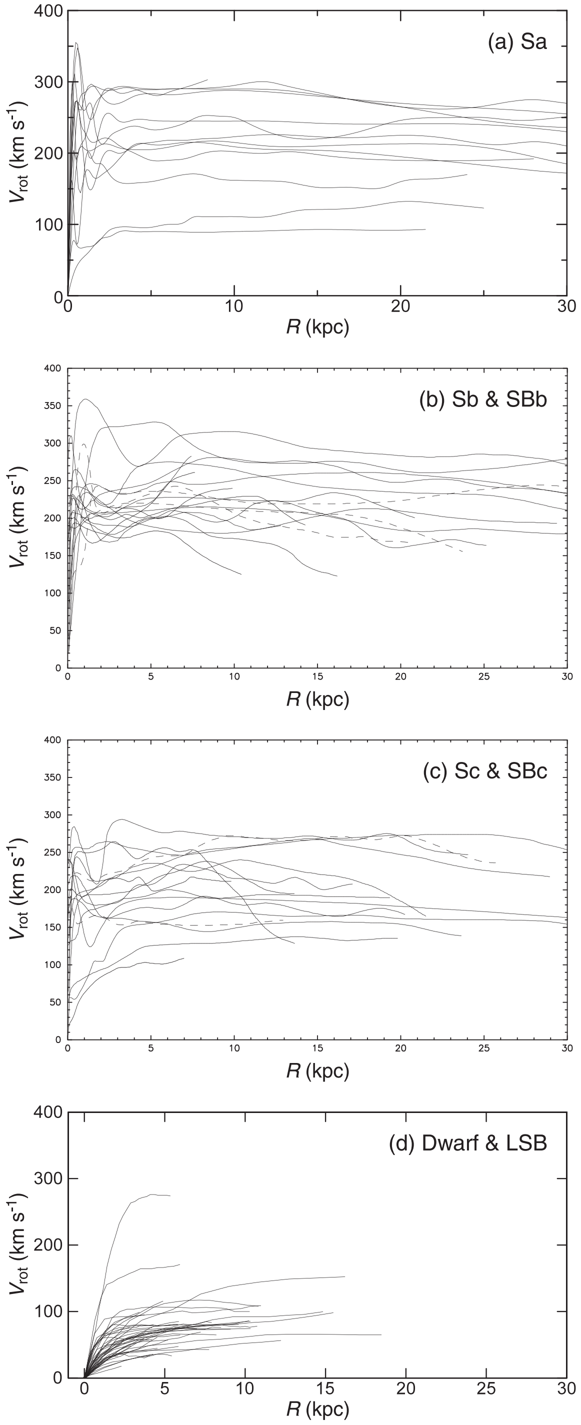

Fig. 15. Rotation curves for Sa-type galaxies (top: Noordermeer et al. 2007), Sb (solid lines) and barred SBb (dashed lines) (second panel), Sc (solid lines) and SBc (dashed lines) (third panel: Sofue et al. 1999), and dwarf and low surface brightness galaxies (bottom: Swaters et al. 2009).

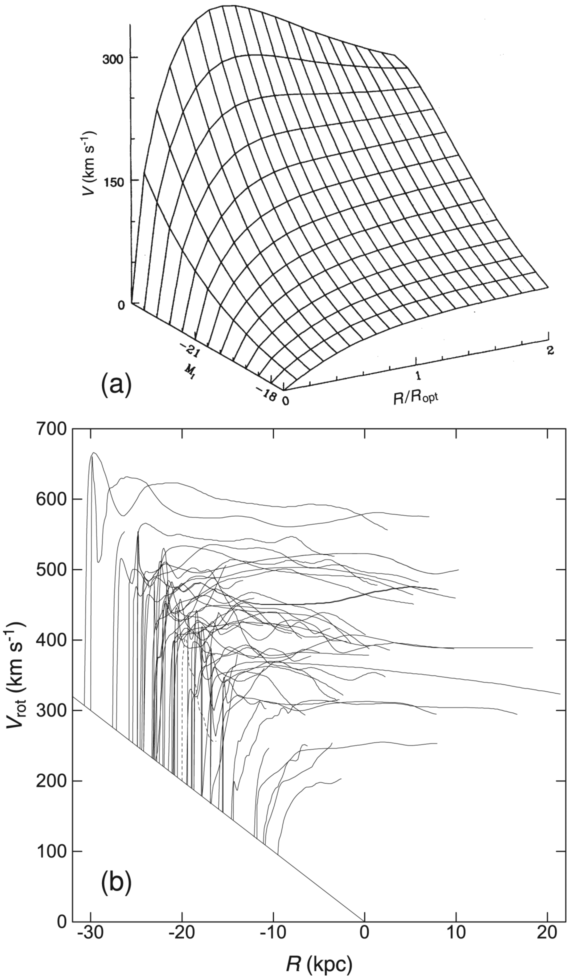

Fig. 16. (a) Universal rotation curves obtained from 967 spiral galaxies (Persic & Salucci 1995). (b) Observed rotation curves from figure 14 with the origins shifted according to the disk rotation velocities (averages from $R = 1$ to 10 kpc), approximately in the order of type, Sa (top-left), Sb, and Sc (bottom-right).

3.4 Galaxy types and rotation curves

3.4.1 Observed rotation curves

Figure 14 shows rotation curves published in the last two decades as compiled from the literature by Sofue (2016), and figure 15 shows those for galaxies types from Sa to Sc. The shapes of disk and halo rotation curves are similar to each other for different morphologies from Sa to Sc, from less-massive to massive galaxies. This suggests that the form of the gravitational potential in the disk and halo is rather universal over the galaxy types.

The examples of rotation curves shown in figure 14 are of nearby spiral galaxies and are obtained by combining optical (mainly Hα) and radio (CO and H I) observations. There is a marked similarity of form in rotation curves for galaxies with different morphologies from Sa to Sc (figure 15). The forms may be classified into three groups: the centrally peaked, shoulder rise, and rigid-body rise types. These three types are observed mainly in massive and large-diameter galaxies, medium-sized galaxies, and less-massive Sc and dwarf galaxies, respectively.

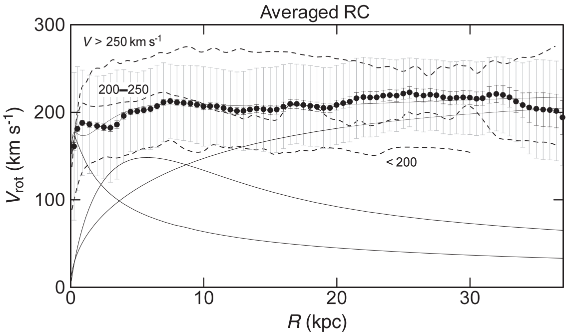

Fig. 17. Black circles show Gaussian-averaged rotation curve from all galaxies listed in Sofue et al. (1999). Long and short bars are standard deviations and standard errors, respectively. Thin lines show the least-χ^2 fitting with the de Vaucouleurs bulge (scale radius 0.57 kpc, mass $9.4 \times 10^9\,M_\odot$), exponential disk (2.7 kpc, $3.5 \times 10^{10}\,M_\odot$), and NFW dark halo (35 kpc, $\rho_0 = 3 \times 10^{-3}\,M_\odot\,\mathrm{pc}^{-3}$). The three dashed lines are the averaged rotation curves of galaxies with maximum velocities of, from top to bottom, greater than 250 km s^{-1}, between 200 and 250 km s^{-1}, and below 200 km s^{-1}, respectively.

3.4.2 Universal rotation curve

Massive Sa to Sb galaxies show higher central velocities than less-massive Sc galaxies (figure 16). In contrast, dwarf galaxies show a slower central rise in a rigid-body fashion. Massive galaxies have universally flat rotation, while less-massive galaxies show a monotonically increasing rotation curve (Persic & Salucci 1991; Persic et al. 1996). The observed rotation curves may be approximated by a simple function (Persic et al. 1996; Courteau 1997; Roscoe 1999) which is dependent on the luminosity and radius of a galaxy in the sense that the more luminous a galaxy, the higher the maximum rotation velocity. It was also shown that the mass-to-luminosity (M/L) ratio is larger for less-massive, hence less-luminous, galaxies. This correlation has also been found to be true for Sc to dwarf galaxies, exhibiting a universal scaling relation between the luminosity and the dark halo mass (Kormendy & Freeman 2016).

3.4.3 Flatness and similarity of rotation curves

The flatness of the overall shape of entire rotation curves applies to any mass range of galaxies. Figure 17 shows averaged rotation curves of galaxies from the sample of Sofue et al. (1999), categorized into three groups by dashed lines: the first group being those with maximum rotation velocity greater than 250 km s^{-1}, the second between 200 and 250 km s^{-1}, and the third slower than 200 km s^{-1}.

The thick line shows a Gaussian-averaged rotation curve of all the sample galaxies, where long and short bars denote the standard deviation and standard error of the mean

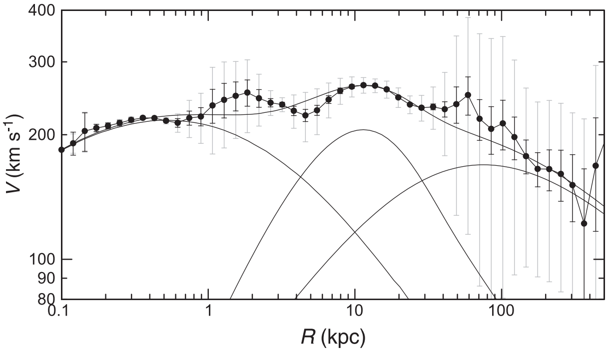

Fig. 18. Logarithmic rotation curve of M 31. Thin lines show the least-χ^2 fit by the bulge, disk and dark halo components.

value, respectively, in each radius bin at 0.5 kpc intervals, with a Gaussian averaging width of 0.5 kpc.

3.5 Dark halo: Grand rotation curves

The outermost rotation curve beyond the flat disk is still not well determined for external galaxies because of the lack of extended disk and weak emissions. In order to solve this difficulty, non-coplanar objects such as outer globular clusters and satellite galaxies have often been used to estimate the dark halo masses via the application of the virial theorem.

Similarly in the case of the Milky Way, orbiting satellite galaxies can be used to obtain expected circular velocities within several hundred kpc of the parent galaxy (Sofue 2013b). The technique has been applied to M 31 to derive a grand rotation curve (GRC) within ∼300 kpc by combining disk rotation velocities and radial velocities of satellite galaxies and of globular clusters. Figure 18 shows the logarithmic GRC and model fitting by bulge, disk, and dark halo components (Sofue 2015). The whole rotation curve up to ∼40 kpc is well represented by the pseudo-isothermal halo model (Burkert 1995), predicting a flat rotation, while the outermost region beyond 50 kpc seems to be better represented by the Navaro–Frenk–White (NFW: Navarro et al. 1996, 1997) model.

3.6 Nuclear rotation curves and black holes

3.6.1 Innermost velocities

Central rotation curves have been produced for a number of galaxies by a systematic compilation of PV diagrams in the Hα and CO lines (Rubin et al. 1997; Sofue et al. 1997, 1998, 1999; Bertola et al. 1998). Many spirals exhibit rapid central velocities, suggesting massive compact nuclear objects (Kormendy & Westpfahl 1989; van der Marel et al. 1994; Kormendy & Richstone 1995; Bertola et al. 1998; Richstone et al. 1998; Ferrarese & Ford 1999; Kormendy & Ho 2013).

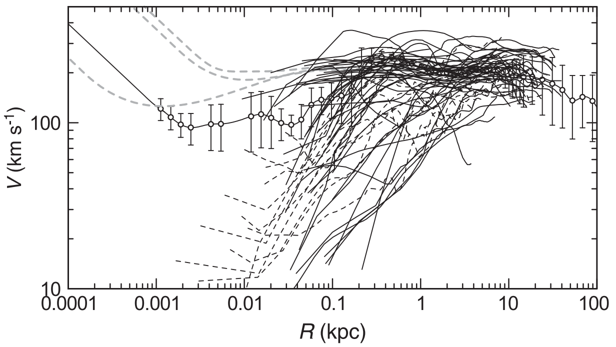

Fig. 19. Logarithmic rotation curves of nearby spiral galaxies with typical resolutions, ∼2″–10″ (thick lines) and those from Virgo CO survey (∼1″, thick dashed lines), compared with the Milky Way rotation curve (circles with error bars). Three gray dashed lines show NGC 224, NGC 1068, and NGC 4258 as interpolated with their black holes by horizontal straight lines.

VLBI water maser observations of the spiral galaxy NGC 4258 showed a disk of radius 0.1 pc in Keplerian rotation, indicating the first firm evidence for a massive black hole of mass $3.9 \times 10^7\, M_\odot$ (Nakai et al. 1993; Watson & Wallin 1994; Miyoshi et al. 1995; Herrnstein et al. 1999). Further VLBI observations of the water maser line have revealed a rapidly rotating nuclear torus of sub-parsec scales in several nearby active galactic nuclei (Haschick et al. 1990; Greenhill et al. 1996; Trotter et al. 1998; Sawada-Satoh et al. 2000).

3.6.2 Logarithmic presentation

Logarithmic presentation of rotation curves is a powerful tool in the discussion of the innermost dynamics in relation to the galactic structure. Figure 19 shows rotation curves of nearby galaxies and Virgo samples in logarithmic presentation. Also are shown the rotation curves of nearby galaxies with known super-massive black holes, where black holes and outer rotation curves are interpolated by dashed lines. The thick line with dots and error bars is the rotation curve of the Milky Way (Sofue 2013b). The figure demonstrates that, except for the Milky Way, the resolution is not sufficient, and higher resolution observations such as using ALMA are a promising subject for the future for linking the central black hole to the galactic structure.

3.6.3 Effect of finite resolution

The simulation in figure 11 reveals the effect of the finite resolution on the observed PV diagram as shown. Central rotation curves derived from observed PV diagrams generally give lower limits to the rotation velocities. Angular resolution and high dynamic range are crucial for the analysis of central kinematics (Rubin et al. 1997; Bertola et al.

1998; Sofue et al. 1998, 1999). Also crucial is the interstellar extinction in the optical observations of the nuclear dusty disks. To avoid this difficulty, radio line observations, particularly CO lines, are powerful because of the negligible extinction and high concentration in the nuclei (Sofue et al. 1999).

3.7 Shapes of rotation curves and galaxy types

Figure 15 shows observed rotation curves of Sa, Sb, Sc, and low-surface-brightness galaxies. The individuality of the observed rotation curves of many spiral galaxies can be explained by the difference in the dynamical parameters of the bulge, disk, and dark halo. Without particular exceptions, the observed rotation curves can be reproduced by properly choosing the masses and scale radii of the mass components.

3.7.1 Sa–Sc galaxies

In each mass component of the bulge, disk, and dark halo, it is known that the larger the scale radius, the more massive the component, and therefore the higher the corresponding rotation velocity (Sofue 2016). This general characteristic applies to the comparison among different galaxies. Thus, the general tendency of rotation curve shapes to differ among the galaxy types can be simply attributed to their mass and size differences. Namely, earlier-type (Sa, Sb) galaxies are generally more massive and larger in size, and hence show higher rotation velocity, than later-type (Sc) galaxies.

The most significant difference in the shape occurs in the central rotation curves: Sa and Sb galaxies, including the Milky Way, have high-velocity rotation near the nucleus, while Sc galaxies show slower and rigid-body-like rotation in the center. This means that Sa and Sb galaxies have large and massive central bulges. In contrast, Sc galaxies have smaller and less massive bulges.

Another difference, though not so significant, appears in the outermost rotation curve: earlier galaxies show flat or slowly declining rotation in the outermost region, while later-type galaxies show monotonically increasing rotation.

3.7.2 Barred galaxies

The kinematics of barred galaxies is complicated due to the non-circular streaming motion superposed on the circular motion (e.g., Bosma 1981a, 1981b). Considering that half, or more than half, of observed galaxies exhibit bars, it is not easy to discuss particular differences of rotation curves between bar and non-bar galaxies. Rotation curves for SBb and SBc galaxies, shown by dashed lines in figure 15, are not particularly distinguishable from those for normal galaxies.

Another effect of bars on rotation curves would be the statistical underestimation of rotation velocity: since interstellar gas is streaming along the bar (Hunter & Cottesman 1996; Buta et al. 1999; Kuno et al. 2000), observed velocities are close to the rigid-body motion of the bar potential, and hence slower than the circular velocity.

Considering the larger probability of side-on viewing of a bar than that for end-on viewing, the rotation velocity simply derived from the radial velocities is statistically underestimated.

For barred galaxies, more sophisticated modeling of non-circular motions is inevitable based on 2D velocity measurements, such as the DISKFIT method proposed by Spekkens and Sellwood (2007), or the numerical method based on *N*-body simulations (Randriamampandry et al. 2015). In fact, in the past decade, extensive 2D spectroscopy has been obtained for a large number of barred spiral galaxies by Fabry–Perot Hα observations (e.g., Dicaire et al. 2008), which will open a new era of non-axisymmetric galactic dynamics, overcoming the difficulties raised in table 3.

3.7.3 Dwarf and low surface brightness (LSB) galaxies

In recent decades, a large number of low surface brightness (LSB) galaxies have been found (Schombert & Bothun 1988; Schombert et al. 1992). Dwarf and LSB galaxies show slow rotation, monotonically rising until their galaxy edges (Carignan & Freeman 1985; de Blok et al. 1996, 2001; Swaters et al. 2000, 2009; Blais-Ouellette et al. 2001; de Blok 2005; Noordermeer et al. 2007). Blue compact galaxies also show rotation curves that rise monotonically to the edges of the galaxies (Östlin et al. 1999). Also, dwarfs with higher central light concentrations have more steeply rising rotation curves, similarly in the case of spirals.

Observations show that the M/L ratio of dwarfs and LSB galaxies is usually higher than that of normal spirals, indicating that they are more dark-matter-dominant than normal spirals (Carignan 1985; Carignan & Freeman 1985; Carignan & Beaulieu 1989; Carignan & Puche 1990a, 1990b; Jobin & Carignan 1990; Lake et al. 1990; Puche et al. 1990, 1991b, 1991a; Broeils 1992; Blais-Ouellette et al. 2001; Carignan et al. 2006).

3.7.4 Interacting and irregular galaxies

Rotation curves for irregular and interacting galaxies are not straightforward. Some irregular galaxies exhibit quite normal rotation curves, whereas some reveal apparently peculiar rotations. Hence, it is difficult to deduce a general law property to describe the curves, but individual cases may be studied case-by-case. We show some examples below.

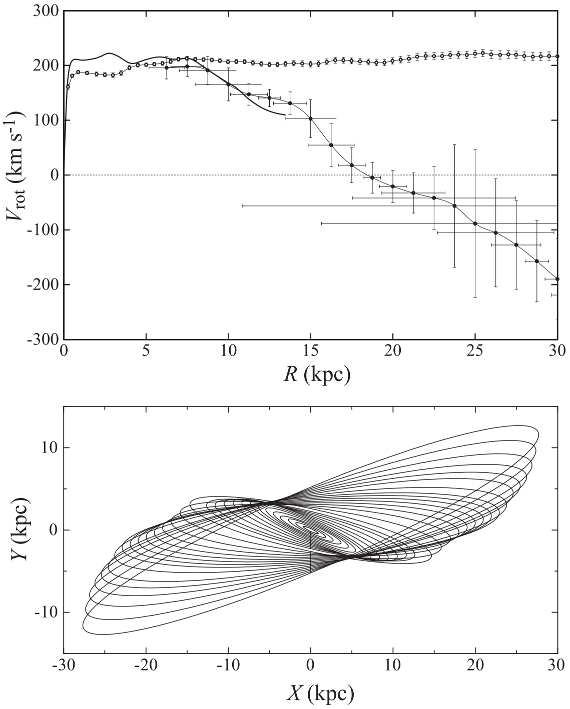

Fig. 20. (Top) Anomalous rotation curve of M 51 showing faster decrease than Keplerian beyond 8 kpc followed by apparent counter rotation, compared with an averaged rotation curve of spiral galaxies. (Bottom) Warped disk calculated for rotation curve assuming a universal rotation. The line-of-sight is toward the top. (Oikawa & Sofue 2014).

The Large Magellanic Cloud is the closest dwarf galaxy interacting with the companion Small Magellanic Cloud and the parent Milky Way. Despite the strong gravitational interaction, the rotation curve is nearly flat at $\sim$100 km s^{-1} (Kim et al. 1998). The dynamical center inferred from the kinematical center is displaced from the optical center of the bar, suggesting a massive component that is not centered by a stellar bulge. The dark bulge suggests an anomalously high M/L ratio in the dynamical center (Sofue 1999).

The peculiar galaxy M 51 (NGC 5194) interacting with the companion NGC 5195 exhibits an anomalous rotation curve, which declines more rapidly than Keplerian rotation curve in the outer disk (figure 20). Even counter-rotation is observed in the outermost H I ring (Rots et al. 1990; Appleton et al. 1986). The kinematics of M 51 has been observed at various wavelengths, which indicates a rotation anomaly. This apparent rotation anomaly is explained by the warping of the galactic disk, assuming that the galaxy intrinsically has a normal flat rotation curve (Oikawa & Sofue 2014). Figure 20 shows a calculated warping of the disk for a given normal rotation curve, where the disk is nearly flat and then bends steeply at $r = 7.5$ kpc.

The peculiar galaxy M 82 is a companion of the giant spiral M 81. It shows an exceptionally peculiar rotation property. It has a normal steep rise and high rotation near the center, but it exhibits a significantly declining rotation, obeying the Keplerian law beyond the peak. This can be well explained and modeled by a tidal truncation of the outer disk and dark halo as a result of a close encounter with the massive parent galaxy M 81.

3.7.5 Activity and rotation curves

Active galaxies, like starburst galaxies, Seyferts, LINERs, and those with nuclear jets, appear to show no particularly peculiar rotation. Even such an active galaxy as NGC 5128 (Cen A) shows a rotation curve similar to a normal galaxy (van Gorkom et al. 1990). The edge-on galaxy NGC 3079 has strong nuclear activity and is associated with bipolar lobes of radio continuum emission and ionized, high-temperature gas. However, its rotation properties are quite normal with very high central velocities (Irwin & Sofue 1992; Sofue & Irwin 1992).

While these galaxies show a steep central rise of the rotation curve, it is not peculiar, but generally observed in normal massive galaxies without any pronounced activity. Thus, the global rotation and mass distribution of active galaxies are considered to be normal. This means that the nuclear activity is not directly produced by the fundamental dynamical structure, but caused by more temporal dynamics and/or ISM phenomena in the central deep gravitational potential, such as a sudden inflow triggered by intermittent feeding of circumnuclear gas and stars.

3.8 Statistical properties of rotation curves: Tully–Fisher relation

Rubin et al. (1985) used their synthetic rotation curves to derive dynamical masses in the interior of the Holmberg radius (R_{25}) of spiral galaxies, and showed their clear correlation with the H-band infrared luminosity. Instead of the total dynamical mass, the maximum rotation velocity at a few galactic-disk scale radii was shown to be related to the luminosity, observed as half of the velocity width of an integrated 21 cm H I line velocity profile. The relation is called the Tully–Fisher relation (Tully & Fisher 1977; Aaronson & Mould 1986; Mathewson et al. 1992; Mathewson & Ford 1996; Masters et al. 2008, 2014), and is one of the major tools for deriving intrinsic luminosities of distant galaxies for measurement of the Hubble constant.

3.9 High-redshift rotation curves

The rotation and dynamics of high-redshift galaxies at cosmological distances are one of the major subjects in the new era of sensitive observations in the 21st century. Rotation curves of sub-z ($z < 1$) galaxies had been observed already in past decades (Vogt et al. 1993, 1996, 1997; Simard & Prichet 1998; Kelson et al. 2000), but the modern era of higher-redshift rotation curves was begun in this century.

Erb et al. (2003) used Keck I, II telescopes and VST (Very Large Telescope Survey Telescope) to obtain near-infrared slit spectra for 16 star-forming galaxies at $z = 2$–3. Referring to archival HST (Hubble Space Telescope) images, they obtained rotation curves for six galaxies. Although the angular resolution, $\sim 0\farcs5$, corresponding to ~ 5 kpc, was not sufficient to resolve the details, the rotation velocities of 100 to 200 $\mathrm{km\,s^{-1}}$ have been observed, and the mean dynamical mass of the galaxies was found to be greater than $4 \times 10^{10}\,M_{\odot}$.

Genzel et al. (2008, 2011) obtained 2D Hα velocity fields for star-forming galaxies at $z = 2$–3, obtaining rotation curves along the major axis for several objects. There is an increasing number of observations of galaxies at $z \sim 1$–3 in the near-infrared spectroscopy using the HST and large-aperture telescopes (Robertson & Bullock 2008; van der Wel & van der Marel 2008; Shapiro et al. 2008; Law et al. 2009; Epinat et al. 2012).

The rotation curve for BzK 6004 at $z = 2.387$ (Genzel et al. 2011) shows a rotation property similar to those in the nearby galaxies. Distant galaxies so far observed at redshifts $z < 3$ appear to show no particular difference in rotation curve shapes or velocities between distant and nearby galaxies. This may imply that the dynamical structure of spiral galaxies at the present time was already reached at these redshifts. Higher-resolution rotation curves at higher redshifts would be crucial in investigating the dynamical evolution of disk galaxies and their merging processes.

However, the inner rotation curves of high-redshift galaxies are still not precise enough to be compared with those of nearby galaxies. This is mainly due to the beam-smearing effect caused by the limited angular resolution of instruments. This effect usually results in a milder rise and slower velocity of rotation in the inner and nuclear regions of the galaxies, as well as in higher velocity dispersion, than the true values. It may be remembered that the angular resolution of $0\farcs01$ achieved by the current optical/infrared/sub-mm instruments corresponds to a linear resolution of only ~ 200 pc at $z > 2$ or at distances greater than several billion pc.

4 Mass distribution in disk galaxies

There are two major methods to measure the mass distribution using rotation curves: the direct method and the decomposition method. In the direct method, the rotation velocity is used to calculate the mass distribution directly. In the decomposition method, a galaxy is represented by the superposition of several mass components, and the rotation curve is fitted by searching for the best-fitting parameters of those components.

4.1 Direct mass determination

By this direct method, the mass distribution in a galaxy is calculated directly from the rotation curve. It is not necessary to give an a priori functional form: only an assumption has to be made, if the galaxy's shape is either a sphere or a flat disk. The "true" mass profile is considered to lie between the two extreme cases of the spherical and axisymmetric disk distribution.

4.1.1 Sphere case

On the assumption of spherical distribution, the mass inside radius R is given by

$$M(R) = \frac{RV(R)^2}{G}. \tag{34}$$

Then the surface-mass density (SMD) $\Sigma_{\mathrm{S}}(R)$ at R is calculated by

$$\Sigma_{\mathrm{S}}(R) = 2\int_0^{\infty} \rho(r) dz. \tag{35}$$

Remembering

$$\rho(r) = \frac{1}{4\pi r^2}\frac{dM(r)}{dr}, \tag{36}$$

the above expression can be rewritten as

$$\Sigma_{\mathrm{S}}(R) = \frac{1}{2\pi}\int_R^{\infty} \frac{1}{r\sqrt{r^2 - R^2}}\frac{dM(r)}{dr} dr. \tag{37}$$

This gives a good approximation for a spheroidal component in the central region, but results in underestimated mass in the outer regions. Particularly, the approximation fails in the outermost region near the end of the rotation curve, due to the edging effect of integration.

4.1.2 Flat-disk case

The SMD of a flat thin disk, $\Sigma_{\mathrm{D}}(R)$, is calculated by solving the Poisson equation on the assumption that the mass is symmetrically distributed in a disk of negligible thickness (Freeman 1970; Binney & Tremaine 1987). It is given by

$$\Sigma_{\mathrm{D}}(R) = \frac{1}{\pi^2 G}\left[\frac{1}{R}\int_0^R \left(\frac{dV^2}{dr}\right)_x K\left(\frac{x}{R}\right) dx + \int_R^{\infty} \left(\frac{dV^2}{dr}\right)_x K\left(\frac{R}{x}\right)\frac{dx}{x}\right]. \tag{38}$$

Here, K is the complete elliptic integral, which becomes very large when $x \simeq R$.

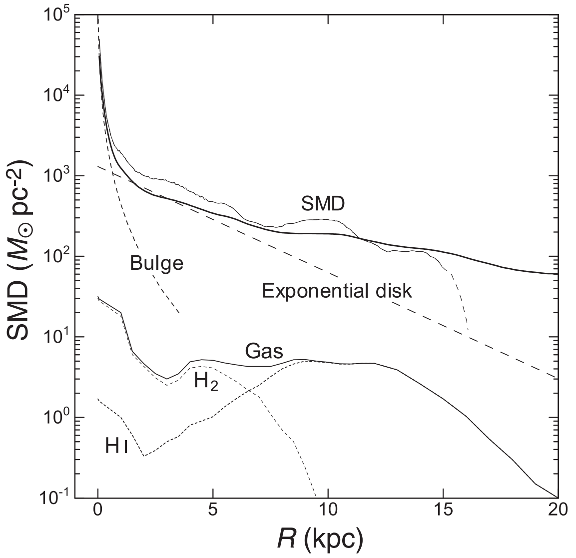

Fig. 21. SMD distribution in the Milky Way. The thick line shows the directly calculated SMD in the thin disk case, and the thin line shows the result in the sphere case. The long-dashed smooth and dashed lines are the model profiles for de Vaucouleurs bulge and exponential disk. The lower lines show the SMD of interstellar gas made by annulus-averaging of figure 7 (Nakanishi & Sofue 2003, 2006, 2016). H I and H_2 gas SMDs are also shown, separately, by dotted lines.

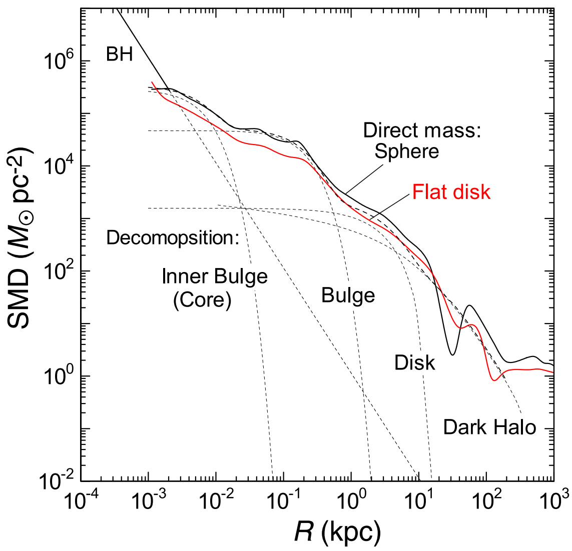

Fig. 22. Directly calculated SMD of the Milky Way under the sphere (thick black line) and flat-disk (thin red line) assumptions on a log–log plot, compared with the result found by the deconvolution method (dashed lines). The straight line represents the black hole with mass 3.6 × 10^6 $M_\odot$. (Color online)

A central black hole may influence the region within ~1, but it does not much affect the galactic scale SMD at lower resolution. Since only a few data points exist in the innermost region, the reliability in there is lower than the outer region. Since the rotation curves are nearly flat or declining outward beyond maximum, the SMD values are usually slightly overestimated in the outer disk.

4.1.3 Milky Way's direct mass calculation

Figure 21 shows SMD distributions in the Galaxy calculated by the direct methods for the sphere and flat-disk cases, compared with SMD calculated for the components obtained by deconvolution of the rotation curve. There is a remarkable similarity between the results from using the direct methods and those obtained by rotation curve deconvolution.

The SMD is strongly concentrated toward the center, reaching as high as $\sim 10^5\,M_\odot\,\mathrm{pc}^2$ within ~10 pc. The galactic disk appears as an exponential disk, as indicated by the straight-line at $R \sim 3$ to 8 kpc on the semi-logarithmic plot. It is worth noting that the dynamical SMD is dominated by dark matter, because the SMD is the projection of the extended dark halo. Note, however, that the volume density in the solar vicinity is dominated by the disk's stellar mass. The outer disk is followed by an outskirt with a slowly declining SMD profile, which indicates the dark halo, extending to the end of the rotation curve measurement.

In figure 21, we also show the radial distribution of interstellar gas density, as calculated by azimuthally averaging the gas density distribution in figure 7. The gas density is much smaller than the dynamical mass density, by an order of magnitude. The SMD of ISM is $\sim 5.0\,M_\odot\,\mathrm{pc}^{-2}$ ($R \sim 8$ kpc), sharing only several percent of the disk mass density $\sim 87.5\,M_\odot\,\mathrm{pc}^{-2}$

The SMDs obtained by deconvolution and direct methods are consistent with each other within a factor of ~1.5. At $R \sim 8$ kpc, the directly calculated SMD is $\sim 300\,M_\odot\,\mathrm{pc}^{-2}$, whereas it is calculated to be ~200–250 $M_\odot\,\mathrm{pc}^{-2}$ by deconvolution, as shown in figure 22.

4.1.4 Spiral galaxies' direct mass

Figure 23 shows SMD distributions of spiral galaxies calculated for the rotation curves shown in figure 14 using the direct methods. The results for the flat-disk assumption give stable profiles in the entire galaxy, while the sphere assumption yields often unstable mass profiles due to the edge effect in the outermost regions. On the other hand, the central regions are better represented by the sphere assumption because of the suspected spherical distribution of mass inside the bulge.

The calculated SMD profiles for galaxies are similar to that for the Milky Way. Namely, dynamical structures represented by the density profiles in spiral galaxies are similar to each other, exhibiting universal characteristics as shown in these figures: high central concentration, exponential disk, and an outskirt due to the dark halo.

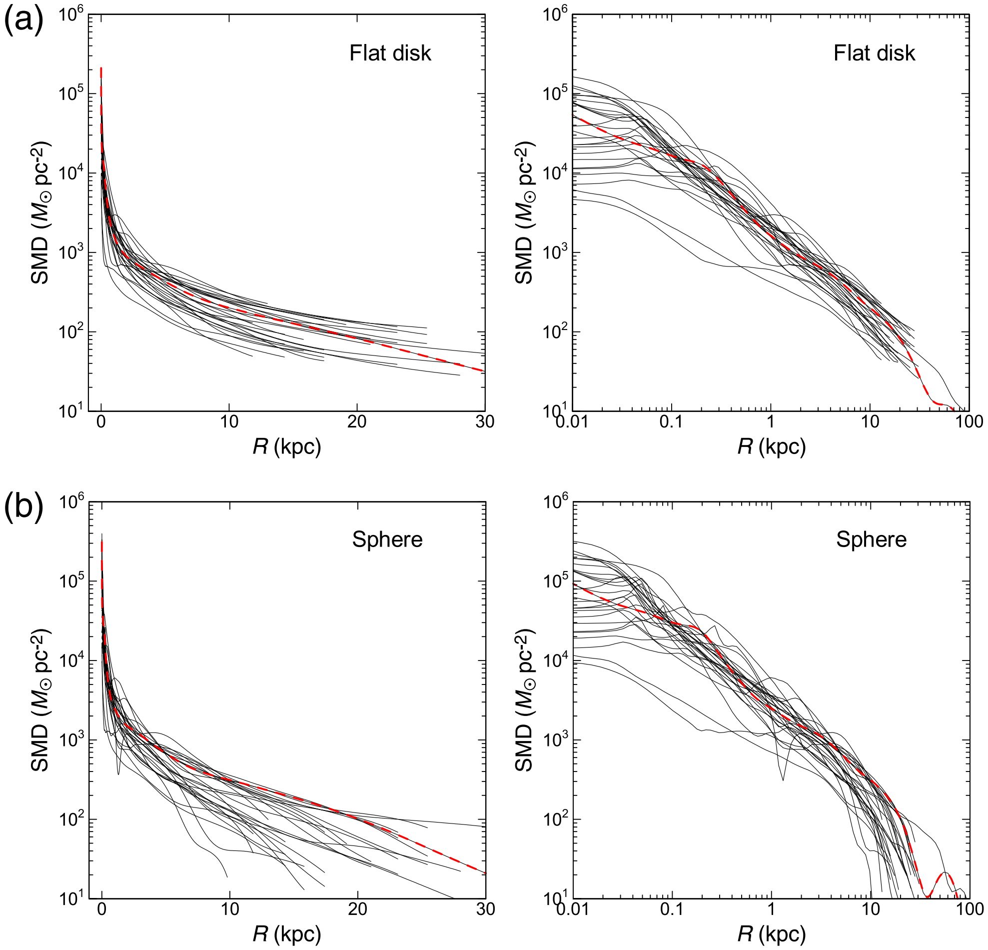

Fig. 23. (a) Direct SMD distributions in spiral galaxies with end radii of RCs greater than 15 kpc (from Sofue 2016) calculated under the flat-disk assumption, and the same distributions in logarithmic radius (Sofue 2016). Red dashed lines indicate the Milky Way. (b) Same as (a), but under the sphere assumption. (Color online)

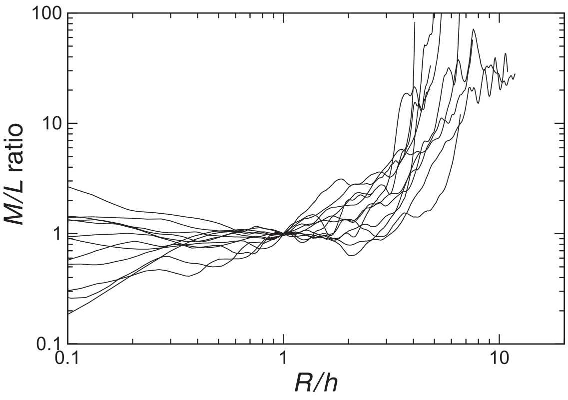

Fig. 24. M/L ratios in spiral galaxies normalized at scale radii using data from Takamiya and Sofue (2000), where L is the optical luminosity.

4.1.5 Mass-to-luminosity ratio

The farthest rotation velocity measured so far for a spiral galaxy is those for the Milky Way and M 31 up to ~300 kpc, where the kinematics of satellite galaxies was used to estimate the circular velocities (Sofue 2012, 2013b). The rotation curve obtained was shown to be fitted with the NFW density profile.

Note, however, that the NFW model predicts declining rotation only beyond galacto-centric distances farther than ~50 kpc. Inside this radius, there is not much difference in the rotation curve shapes of NFW model and isothermal model, predicting almost flat (NFW) or perfectly flat (isothermal) rotation. Practically, for most galaxies with rotation curves up to ~30 kpc, both models yield much the same result about their halos. In either model, observed rotation velocities in spiral galaxies show that the mass in their halos is dominated by dark matter.

The M/L ratio can be obtained by dividing the SMD by surface luminosity profiles (Forbes 1992; Takamiya & Sofue 2000; Vogt et al. 2004b). Figure 24 shows M/L ratios for various spiral galaxies normalized at their scale radii (Takamiya & Sofue 2000). While the M/L ratio is highly variable inside their disk radii, it increases monotonically with the close vicinity of the galaxies' edges. However, for the outermost halos farther than ~20–30 kpc, beyond the

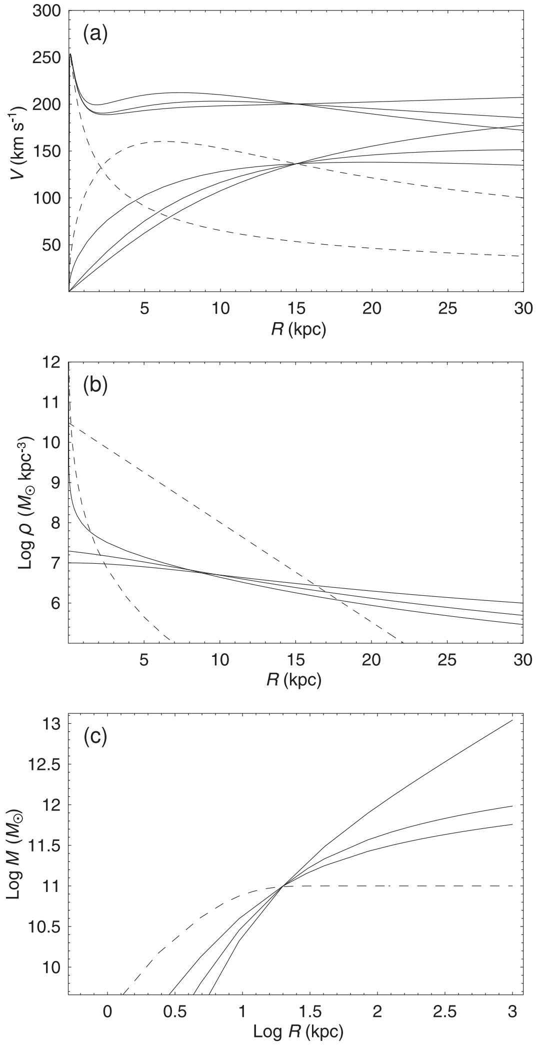

Fig. 25. (a) Analytic rotation curves composed of bulge, disk, and dark halo components represented by isothermal, Burkert (1995), and NFW models (upper solid lines from top to bottom at $R = 30$ kpc). Dashed lines represent the de Vaucouleurs bulge and exponential disks and three lower solid lines represent the halos as above. (b) Corresponding volume densities. (c) Corresponding enclosed mass within radius r.

plotted radii in the figure, it is extremely difficult to determine the M/L ratio from observations because of the limited finite radii of the luminous disks, beyond which the surface brightness is negligibly low, and hence the M/L ratio tends to increase in value infinitely.

4.2 Rotation curve decomposition into mass components

4.2.1 Superposition of mass components

The rotation velocity is written using the gravitational potential as

$$V(R) = \sqrt{R\frac{\partial \Phi}{\partial R}}, \tag{39}$$

where

$$\Phi = \Sigma \Phi_i, \tag{40}$$

with Φ_i being the potential of the ith mass component. Knowing that $V_i(R) = \sqrt{R\partial\Phi_i/\partial R}$, we have

$$V(R) = \sqrt{\Sigma V_i^2}. \tag{41}$$

It is often assumed that there are multiple components that are the central black hole, a bulge, a disk, and a dark halo:

$$V(R) = \sqrt{V_{\rm BH}(R)^2 + V_{\rm b}(R)^2 + V_{\rm d}(R)^2 + V_{\rm h}(R)^2}. \tag{42}$$

Here, subscripts BH, b, d, and h represent black hole, bulge, disk, and dark halo, respectively. Figure 25 shows a schematic rotation curve and its decomposition into four mass components.

The parameters (masses and scale radii of individual components) are iteratively determined by the least-χ^2 fitting (Carignan 1985; Carignan & Freeman 1985). First, an approximate set of parameters is given as an initial condition, where the values of the parameters are hinted by the luminosity profiles of the bulge and disk, and by the shape and amplitude of the rotation curve for the dark halo. All the parameters are fitted simultaneously.

When precise rotation curves are available with a larger number of data points, particularly in the resolved innermost regions of the Milky Way and nearby galaxies, the fitting may be divided into several steps according to the components, in order to save computation time (Sofue 2012). The time per iteration is proportional to nN, where n is the number of data points and N is the number of combination of parameters. The combination number is given by $N = (\Sigma_i n_i)!$, where n_i is the number of parameters of the ith component. On the other hand, it is largely reduced to $N = \Sigma_i(n_i!)$ in the step-by-step method.

Also, it is useful for dividing the fitting radii depending on the component's properties. Namely, a black hole and bulge may not be fitted to data beyond the disk, e.g., beyond $R \sim 10$ kpc, while a halo may not be fitted at $\lesssim 1$ kpc. This procedure can save not only time, but also avoid the degeneracy problem (Bershady et al. 2010a, 2010b). Degeneracy happens for data with low resolution and a small number of measurements, often in old data, in such a way that a rotation curve is represented equally by any of the mass models, or, the data are fitted either with a single huge bulge or disk, or with a single tiny halo.

In the step-by-step method, first, a set of parameters is assumed as the initial condition (as above). The fitting is started individually from the innermost component that has the steepest rise (gradient), which is particularly necessary when a black hole is included. Next, the steeply rising part is

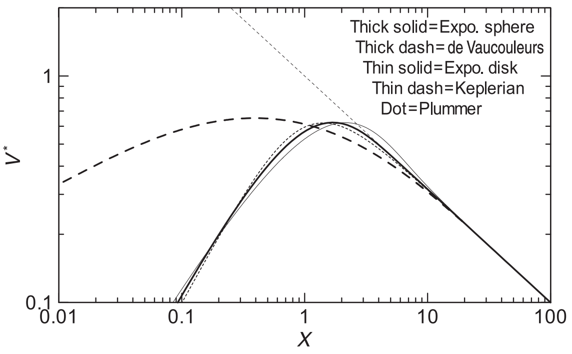

Fig. 26. Comparison of normalized rotation curves for the exponential spheroid, the de Vaucouleurs spheroid, and other typical models, for a fixed total mass. The exponential spheroid model is almost identical to that for the Plummer law model. The central rise of the de Vaucouleurs curve is proportional to $r^{1/2}$, while the other models show a central velocity rise $\propto r$.

fitted with the bulge, and then gradual-rising and flat parts are fitted with the disk. Finally, the residual outskirt is fitted with a dark halo. This procedure is repeated iteratively, starting again from the innermost part, until the χ^2 value is minimized.

Observed rotation curves in spiral galaxies may be usually fitted with three components of the bulge, disk, and dark halo. In the Milky Way, the rotation curve may be better represented by four or five components, which are the central black hole, multiple bulges, an exponential disk, and dark halo.

4.2.2 Massive black hole

The Galactic Center of the Milky Way is known to host a massive black hole, and the mass has been observed to be $M_{\rm BH} = (2.6\text{–}4.4) \times 10^6\, M_\odot$ (Genzel et al. 1994, 1997, 2000, 2010), $(4.1\text{–}4.3) \times 10^6\, M_\odot$ (Ghez et al. 1998, 2005, 2008), and $3.95 \times 10^6\, M_\odot$ (Gillessen et al. 2009).

A more massive black hole has been observed in the nucleus of the spiral galaxy NGC 4258, with a mass of $3.9 \times 10^7\, M_\odot$ (Nakai et al. 1993; Miyoshi et al. 1995; Herrnstein et al. 1999), from VLBI observations of the water maser lines. Some active galaxies have been revealed to nest rapidly rotating nuclear torus of sub-parsec scales indicating massive black holes, and an increasing amount of evidence for massive black holes in galactic nuclei has been reported. Statistics show that the mass (luminosity) of a bulge is positively related to the mass of the central black hole (Kormendy & Westpfahl 1989; Kormendy & Ho 2013).

4.2.3 de Vaucouleurs bulge

The most commonly used profile to represent the central bulge is the de Vaucouleurs (1958) law (figure 26), which was originally expressed by a surface-brightness distribution at projected radius R by

$$\log\beta = -\gamma(\alpha^{1/4} - 1), \tag{43}$$

where $\gamma = 3.3308$. Here, $\alpha = R/R_{\rm b}$ is the normalized radius by the bulge scale radius $R_{\rm b}$, and $\beta = B_{\rm b}(R)/B_{\rm be}$ is the normalized surface-brightness at $R = R_{\rm b}$ by $B_{\rm be} = B_{\rm b}(R_{\rm b})$.

The same de Vaucouleurs profile for the surface mass density is usually adopted for the surface mass density as

$$\Sigma_{\rm b}(R) = \lambda_{\rm b} B_{\rm b}(R) = \Sigma_{\rm be} \exp\left\{-\kappa\left[\left(\frac{R}{R_{\rm b}}\right)^{1/4} - 1\right]\right\}. \tag{44}$$

Here, $\kappa = \gamma \ln 10 = 7.6695$, and $\lambda_{\rm b}$ is the M/L ratio, assumed to be constant, and $\Sigma_{\rm be}$ is the surface mass density at the scale radius $R = R_{\rm b}$. Note that the central value $\Sigma_{\rm bc}$ attains a much higher value than the scaling value $\Sigma_{\rm be}$ as $\Sigma_{\rm bc} = \Sigma_{\rm b}(R = 0) = 2142.0\Sigma_{\rm be}$.

Equations (43) and (44) show that the central SMD at $R = 0$ attains a finite value, and the SMD decreases steeply outward near the center. However, the decreasing rate gets much milder at large radii, and the SMD decreases slowly, forming an extended outskirt (de Vaucouleurs 1958).

The cylindrical mass inside R is calculated by

$$M_{\rm b:cyl}(R) = 2\pi \int_0^R x\Sigma_{\rm b}(x)dx. \tag{45}$$

The total mass of the bulge is given by

$$M_{\rm bt} = 2\pi \int_0^\infty R\Sigma_{\rm b}(R)dR = \eta R_{\rm b}^2 \Sigma_{\rm be}, \tag{46}$$

with $\eta = 22.665$. A half of the total projected (cylindrical) mass is equal to the mass inside a cylinder of radius $R_{\rm b}$.

The volume mass density $\rho(r)$ at radius r for a spherical bulge is now given by

$$\rho(r) = \frac{1}{\pi} \int_r^\infty \frac{d\Sigma_{\rm b}(x)}{dx} \frac{1}{\sqrt{x^2 - r^2}} dx. \tag{47}$$

The circular velocity is thus given by the Kepler velocity of the mass inside R as

$$V_{\rm b}(R) = \sqrt{\frac{GM_{\rm b:sph}(R)}{R}}, \tag{48}$$

where

$$M_{\rm b:sph}(R) = 4\pi \int_0^R r^2 \rho(r)dr. \tag{49}$$

Note that the spherical mass $M_{\rm b:\,sph}(R)$ is smaller than the cylindrical mass $M_{\rm b:\,cyl}(R)$ given by equation (45). At large radii, the velocity approximately decreases in line with

Keplerian law. Figure 26 shows the variation of circular velocity for a de Vaucouleurs bulge.

The de Vaucouleurs law has been extensively applied to fit spheroidal components of late-type galaxies (Noordermeer et al. 2007; Noordermeer 2008). Sérsic (1968) has modified the law to a more general form: $e^{-(R/r_e)^n}$. The de Vaucouleurs and Sérsic laws were fully discussed in relation to their dynamical relation to the galactic structure based on the more general profile (Ciotti 1991; Trujillo 2002). The de Vaucouleurs law has also been applied to fit the central rotation curve of the Milky Way, as shown in figure 4. However, it was found that the de Vaucouleurs law cannot reproduce the observations inside ~200 pc.

It is interesting to see the detailed behavior of the de Vaucouleurs law. At the center, Σ reaches a constant, and volume density varies as $\propto 1/r$, leading to circular velocity $V \propto r^{1/2}$ near the center. Thus, the rotation velocity rises very steeply with infinite gradient at the center. It should be compared with the mildly rising velocity as $V \propto r$ in the other models. Figure 26 shows the difference in normalized behavior of rotation velocity between de Vaucouleurs and other models.

The de Vaucouleurs rotation curve shows a much broader maximum in logarithmic plot compared to the other models, because the circular velocity rises as $V \propto \sqrt{M(<r)/r} \sim \sqrt{r}$. This particular behavior can be better recognized by comparing the half-maximum logarithmic velocity width with other models, where the width is defined by

$$\Delta_{\log} = \log\frac{r_2}{r_1}. \tag{50}$$

Here, r_2 and r_1 ($r_2 > r_1$) are the radii at which the rotational velocity becomes half the maximum velocity. From the figure, we obtain $\Delta_{\log} = 3.0$ for de Vaucouleurs, and $\Delta_{\log} = 1.5$ for the other models, as described later. Thus the width of the de Vaucouleurs's logarithmic curve is twice that of the others, and its shape is much milder.

4.2.4 Other bulge models

Since it was shown that the de Vaucouleurs law fails to fit the observed central rotation, another model has been proposed, called the exponential sphere model. In this model, the volume mass density ρ is represented by an exponential function of radius r with a scale radius a as

$$\rho(r) = \rho_c e^{-r/a}. \tag{51}$$

The mass enclosed within this sphere of radius r is given by

$$M(R) = M_0 F(x), \tag{52}$$

where $x = r/a$ and

$$F(x) = 1 - e^{-x}(1 + x + x^2/2). \tag{53}$$

The total mass is given by

$$M_0 = \int_0^\infty 4\pi r^2 \rho dr = 8\pi a^3 \rho_c. \tag{54}$$

The circular rotation velocity is then calculated by

$$V(r) = \sqrt{GM/r} = \sqrt{\frac{GM_0}{a} F\left(\frac{r}{a}\right)}. \tag{55}$$

In this model the rotational velocity has a narrower peak near the characteristic radius in the logarithmic plot as shown in figure 26. Note that the exponential-sphere model is nearly identical to that for Plummer's law, and the rotation curves have almost identical profiles. In this context, the Plummer law can be used to fit the central bulge components in place of the present models.

4.2.5 Exponential disk

The galactic disk is represented by an exponential disk (Freeman 1970), where the surface mass density is expressed as

$$\Sigma_d(R) = \Sigma_{dc} \exp(-R/R_d). \tag{56}$$

Here, Σ_{dc} is the central value and R_d is the scale radius. The total mass of the exponential disk is given by $M_{disk} = 2\pi \Sigma_{dc} R_d^2$. The rotation curve for a thin exponential disk is expressed by (Binney & Tremaine 1987)

$$\begin{aligned} V_{d(R)} &= \sqrt{R\frac{\partial \Phi}{\partial R}} \\ &= \sqrt{4\pi G \Sigma_0 R_d y^2 \left[I_0(y)K_0(y) - I_1(y)K_1(y)\right]}, \end{aligned} \tag{57}$$

where $y = R/(2R_d)$, and I_i and K_i are the modified Bessel functions.

If the surface mass density does not obey the exponential law, the gravitational force $f(R)$ can be calculated by integrating the x-directional force caused by mass element $\Sigma'_d(x)dxdy$ in the Cartesian coordinates (x, y):

$$f(R) = G \int_{-\infty}^{\infty} \int_{-\infty}^{\infty} \frac{\Sigma_d(x)(R - x)}{s^3} dxdy, \tag{58}$$

where $s = \sqrt{(R - x)^2 + y^2}$. The rotation velocity is then given by

$$V_d(R) = \sqrt{fR}. \tag{59}$$

This formula can be used for any thin disk with an arbitrary SMD distribution $\Sigma(x, y)$, even if it includes non-axisymmetric structures.

4.2.6 Isothermal and NFW dark halos

Evidence for dark matter halo. The existence of dark halos in spiral galaxies has been firmly proved from the well-established difference between the galaxy mass predicted by the luminosity and the galaxy mass predicted by the rotation velocities (Bosma 1981a, 1981b; Rubin et al. 1982a, 1982b, 1985, 1991, 1997, 1999; Kent 1986; Salucci & Frenk 1989; Persic & Salucci 1990; Forbes 1992; Persic et al. 1996; Héraudeau & Simien 1997; Takamiya & Sofue 2000).

In the Milky Way, extensive analyses of the motion of non-disk objects such as globular clusters and dwarf galaxies in the Local Group have shown flat rotation up to ∼100 kpc, and then declining rotation up to ∼300 kpc (Sofue 2013b, 2016). Measurements of outer rotation velocities have made it possible to analyze the extended distribution of the massive dark halo, which is found to fill the significantly wide space in the Local Group. Bhattacharjee et al. (2013) and Bhattacharjee, Chaudhury, and Kundu (2014) have analyzed non-disk tracer objects to derive the outer rotation curve up to 200 kpc in order to constrain the dark matter mass of the Galaxy, reaching a consistent result. As will be shown later, the dark halos of the Milky Way and M 31 are shown to be better represented by the NFW model than by the isothermal halo model.

Isothermal halo.
The simplest model for the flat rotation curve is the semi-isothermal spherical distribution (Kent 1986; Begeman et al. 1991), where the density is written as

$$\rho_{\rm iso}(R) = \frac{\rho^0_{\rm iso}}{1 + (R/h)^2}, \quad (60)$$

where $\rho^0_{\rm iso}$ and $h = R_{\rm h}$ are the central mass density and scale radius, respectively. The circular velocity is given by

$$V_h(R) = V_\infty \sqrt{1 - \left(\frac{h}{R}\right) \tan^{-1}\left(\frac{R}{h}\right)}, \quad (61)$$

which approaches a constant rotation velocity V_∞ at large distances. At small radius, $R \ll h$, the density becomes nearly constant, equal to $\rho^0_{\rm iso}$, and the enclosed mass increases steeply as $M(R) \propto R^3$. At large radii, the density decreases with $\rho_{\rm iso} \propto R^{-2}$. The enclosed mass increases almost linearly with radius as $M(R) \propto R$.

Navarro–Frenk–White (NFW) model.
The most popular model for the dark halo is the NFW model (Navarro et al. 1996, 1997) empirically obtained from numerical simulations in the cold dark matter scenario of galaxy formation. Burkert's (1995) modified model is also used when the singularity at the nucleus is to be avoided. The NFW density profile is written as

$$\rho_{\rm NFW}(R) = \frac{\rho^0_{\rm NFW}}{(R/h)/[1 + (R/h)^2]}. \quad (62)$$

The circular velocity is equal to

$$V_h(R) = \sqrt{\frac{GM_h(R)}{R}}, \quad (63)$$

where M_h is the enclosed mass within the scale radius h.

At $R \ll h$, the NFW density profile behaves as $\rho_{\rm NFW} \propto 1/R$, yielding an infinitely increasing density toward the center, and the enclosed mass behaves as $M(R) \propto R^2$. Burkert's modified profile tends to have a constant density $\rho^0_{\rm Bur}$, similar to the isothermal profile.

At large radius the NFW shows a density profile as $\rho_{\rm NFW,Bur} \propto R^{-3}$, yielding a logarithmic increase in mass, $M(R) \propto \ln R$ (figure 25). Figure 25 shows density distributions for the isothermal, Burkert, and NFW models.

4.2.7 Plummer and Miyamoto–Nagai potential

The current mass models described above do not necessarily satisfy Poisson's equation, and hence, they are not self-consistent in representing a dynamically relaxed self-gravitating system. In order to avoid this inconvenience, Plummer-type potentials are often employed to represent the mass distribution.

The Miyamoto and Nagai's (1975) (MN) potential is one of the most convenient Plummer-type formulae to describe a disk galaxy's potential and mass distribution in an analytic form:

$$\Phi = \sum_{i=1}^{n} \frac{-GM_i}{\sqrt{R^2 + (a_i + \sqrt{z^2 + b_i^2})^2}}, \quad (64)$$

where M_i, a_i, and b_i are the mass, scale radius, and height of the ith spheroidal component, respectively. The rotation velocity in the galactic plane at $z = 0$ is given by

$$V_{\rm rot}(R) = R\sqrt{\sum_{i=1}^{n} \frac{GM_i}{[R^2 + (a_i + b_i)^2]^{3/2}}}. \quad (65)$$

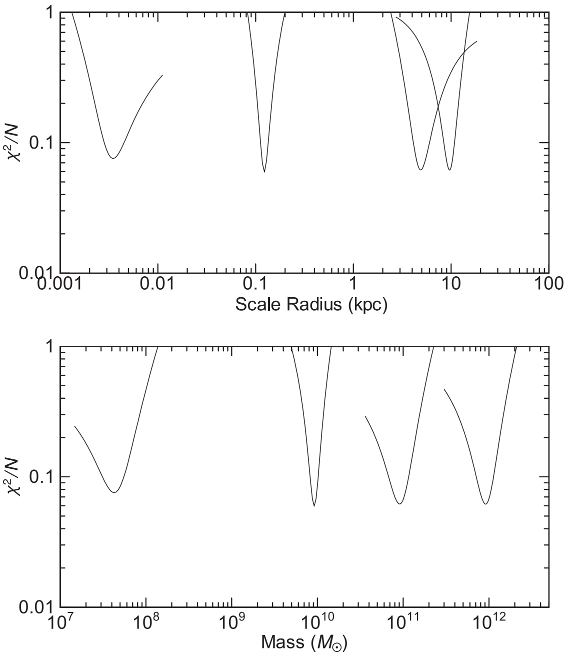

Fig. 27. χ^2 plots around the best-fitting values of the scale radii of the deconvolution components to obtain figure 4.

The mass distribution is given by Poisson's equation:

$$\begin{aligned}\rho(R, z) &= -\frac{\Delta\Phi}{4\pi G} \\ &= \frac{1}{4\pi}\sum_{i=1}^{n} b_i^2 M_i \\ &\quad \times \frac{a_i R^2 + (a_i + 3\sqrt{z^2 + b_i^2})(a_i + \sqrt{z^2 + b_i^2})^2}{[R^2 + (a_i + \sqrt{z^2 + b_i^2})^2]^{5/2}(z^2 + b_i^2)^{3/2}}. \end{aligned} \tag{66}$$

This model was used to approximate the observed rotation curve of the Milky Way (Miyamoto & Nagai 1975). Their proposed parameters are often used to represent a bulge and disk for numerical simulations not only in the original form, but also through adding a larger number of components by choosing the masses and scale radii properly. The original parameters were given as $M_{\rm bulge} \sim 2.05 \times 10^{10}\,M_\odot$, $a_{\rm bulge} = 0$, and $b_{\rm bulge} \sim 0.495\,$kpc, and $M_{\rm disk} \sim 2.547 \times 10^{11}\,M_\odot$, $a_{\rm disk} \sim 7.258\,$pc, and $b_{\rm disk} \sim 0.520\,$kpc.

4.2.8 Degeneracy problem

The models described here are expressed by single-valued simple analytic functions. Each of the functions has only two parameters (mass and size). The black hole is expressed by the Keplerian law with only one parameter (mass). The mass and scale radius of the de Vaucouleurs law are uniquely determined, if there are two measurements of velocities at two different radii. This is also applied to each of the exponential disk and NFW halo.

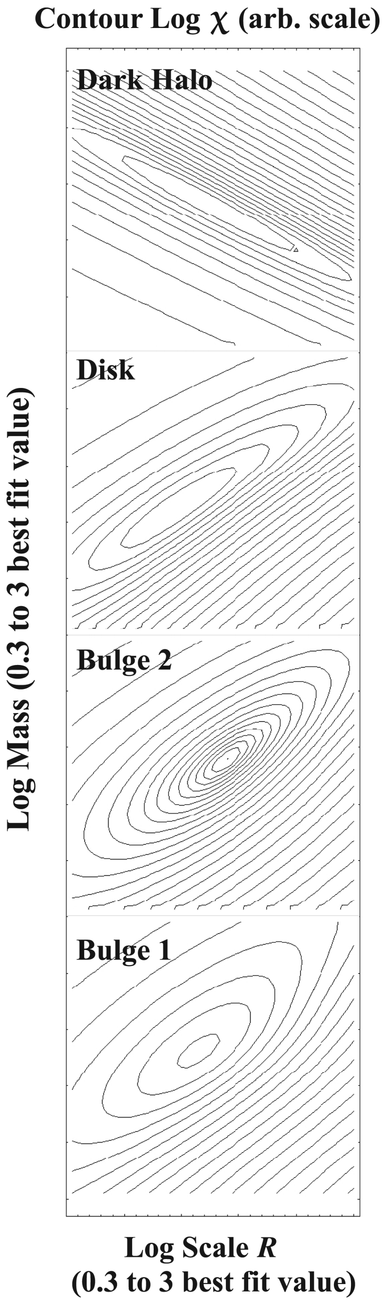

Fig. 28. Contour presentation of the 2D distribution of the log χ^2 value around the best-fitting points in the scale radius–mass space to obtain figure 4.

If the errors are sufficiently small, the three major components (bulge, disk, and halo) can be uniquely determined by observing six velocity values at six different radii. In actual observations, the number of data points is much larger, while the data include measurement errors. Hence, the parameters are determined statistically, by applying the least-squares fitting method or the least-χ^2 method. Thereby, the most likely sets of the parameters are chosen as the decomposition result.

Table 6. Parameters for the mass components of the Galaxy (Sofue 2013b).*

Mass component	Quantities
Black hole	$M_{\rm bh} = 3.6 \times 10^6\, M_\odot$ †
Bulge 1 (massive core)	$a_{\rm b} = 3.5 \pm 0.4$ pc $M_{\rm b} = 0.4 \pm 0.1 \times 10^8\, M_\odot$
Bulge 2‡ (main bulge)	$a_{\rm b} = 120 \pm 3$ pc $M_{\rm b} = 0.92 \pm 0.02 \times 10^{10}\, M_\odot$
Disk	$a_{\rm d} = 4.9 \pm 0.4$ kpc
Dark halo	$M_{\rm d} = 0.9 \pm 0.1 \times 10^{11}\, M_\odot$ $h = 10 \pm 0.5$ kpc $\rho_0 = 2.9 \pm 0.3 \times 10^{-2}\, M_\odot\,{\rm pc}^{-3}$ $M_{R\,<\,200{\rm kpc}} = 0.7 \pm 0.1 \times 10^{12}\, M_\odot$ $M_{R\,<\,385{\rm kpc}} = 0.9 \pm 0.2 \times 10^{12}\, M_\odot$
DM density at the Sun	$\rho_8 = 0.011 \pm 0.001\, M_\odot\,{\rm pc}^{-3}$ $= 0.40 \pm 0.04\,{\rm GeV\,cm}^{-3}$

*The adopted Galactic constants are $(R_0,\ V_0) = (8\,{\rm kpc},\ 238\,{\rm km\,s}^{-1})$ (Honma et al. 2012).

†Genzel et al. (2000, 2008), Genzel, Eisenhauer, and Gillessen (2010).

‡$M_{\rm b}$ is the surface mass enclosed in a cylinder of radius $a_{\rm b}$, but not a spherical mass.

However, when the errors are large and the number of observed points is small, the degeneracy problem becomes serious (Bershady et al. 2010a, 2010b), as the fitting is not unique. Such a peculiar case sometimes happens, when the rotation curve is mildly rising and tends to the flat end, so that the curves are fitted in almost the same statistical significance either with a disk and halo, with a single disk, or with a single halo. Such a mild rise of central rotation is usually observed in low-resolution measurements.

4.3 Rotation curve decomposition in the Milky Way

Observed mass components in the Galaxy and spiral galaxies are often expressed by empirical functions derived by surface photometry of the well-established bulge and disk. Also, the central black hole and the outermost dark halo are inevitable components in order to describe resolved galactic structures.

4.3.1 Black hole, bulge, disk, and halo of the Milky Way

In the rotation curve decomposition in the Milky Way, the following components have been assumed (Sofue 2013b).

1. A central black hole with mass $M_{\rm BH} = 4 \times 10^6\, M_\odot$.
2. An innermost spheroidal component with an exponential-sphere density profile, or a central massive core.
3. A spheroidal bulge with an exponential-sphere density profile.
4. An exponential flat disk.
5. A dark halo with an NFW profile.

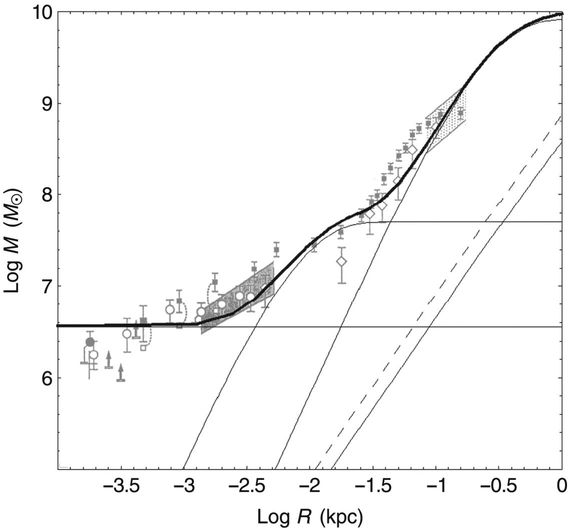

Fig. 29. Enclosed mass calculated for the Galaxy's rotation curve compared to those from Genzel, Hollenbach, and Townes (1994). The horizontal line, thin curved lines, dashed line, and lower straight line indicate the black hole, inner bulge, main bulge, disk, and dark matter cusp, respectively.

The approximate parameters initially given were adjusted to lead to the best-fitting values using the least-χ^2 method. Figure 4 shows the fitting rotation curve, which satisfactorily represents the entire rotation curve from the central black hole to the outer dark halo. Figures 27 and 28 show the variation of χ^2 values around the best-fitting parameters.

The fitting values of the two peaks of rotation curve at $r \sim 0.01$ kpc and $\sim$0.5 kpc are well reproduced by the two exponential spheroids. The figures also demonstrate that the exponential bulge model is better than the de Vaucouleurs model. It must be mentioned that the well-known de Vaucouleurs profile cannot be fitted to the Milky Way's bulge, while it is still a good function for fitting the bulges in extragalactic systems. Table 6 lists the fitting parameters for the Milky Way.

4.3.2 The Galactic Center

Figure 29 shows the enclosed mass in the Galactic Center as a function of radius calculated for the parameters obtained by rotation curve decomposition. The plots are compared with the measured values at various radii, as compiled by Genzel, Hollenbach, and Townes (1994), where their data have been normalized to $R_0 = 8.0$ kpc. It should be stressed that both the plots are in good agreement with each other. The figure shows that the bulge density near the center tends to a constant value, so that the innermost enclosed mass behaves as $\propto r^3$, as the straight part of the plot indicates.

Table 7. Local dark matter density ρ_s near the Sun in the Galaxy from the literature.

Source	ρ_s (GeV cm^{-3})
Weber and de Boer (2010)	0.2–0.4
Salucci et al. (2010)	0.43 ± 0.10
Bovy and Tremaine (2012)	0.3 ± 0.1
Piffl et al. (2014)	0.58
Sofue (2013b), $V_0 = 200\,\mathrm{km\,s^{-1}}$	0.24 ± 0.03
Sofue (2013b), $V_0 = 238\,\mathrm{km\,s^{-1}}$	0.40 ± 0.04
Pato and Iocco (2015) and Pato et al. (2015), $V_0 = 230\,\mathrm{km\,s^{-1}}$	0.42 ± 0.25

On the other hand, the disk has a constant surface density near the center, and hence the enclosed mass varies as $\propto r^2$, as the straight line for the disk indicates. The NFW model predicts a high-density cusp near the center with enclosed surface mass $\propto r^2$, as shown by the dashed line, exhibiting similar behavior to the disk.

4.3.3 Local dynamical values and dark matter density

The local value of the volume density of the disk can be calculated by $\rho_\mathrm{d} = \Sigma_\mathrm{d}/(2z_0)$, where z_0 is the vertical scale height at radius $R = R_0$, when the disk scale profile is approximated by $\rho_\mathrm{d}(R_0, z) = \rho_\mathrm{d0}(R_0)\mathrm{sech}(z/z_0)$. The disk thickness has been observed to be $z_0 = 144 \pm 10$ pc for late-type stars using the Hipparcos catalogue (Kong & Zhu 2008), while a larger value of 247 pc is often quoted as the traditional value (Kent et al. 1991).

The local volume densities of the bulge and dark halo are $\sim 10^{-4}$ and $\sim 10^{-2}$ times the disk density, respectively. However, the SMD projected on the galactic plane of the bulge contributes to 1.6% of the disk value. It is interesting to note that the SMD of the dark halo exceeds the SMD of the disk by several times.

The NFW model was found to fit the Ground Rotation Curve (GRC) quite well (Sofue 2012), including the declining part in the outermost rotation at $R \sim 40$–400 kpc. The local dark matter density is a key quantity in laboratory experiments for direct detection of the dark matter. Using the best-fitting parameters for the NFW model, the local dark matter density in the solar neighborhood is calculated to be $\rho_0^\odot = 0.235 \pm 0.030\,\mathrm{GeV\,cm^{-3}}$. This value may be compared with the values obtained by the other authors as listed in table 7.

4.4 Decomposition of galaxies' rotation curves

4.4.1 Bulge, disk, and NFW halo decomposition of spiral galaxies

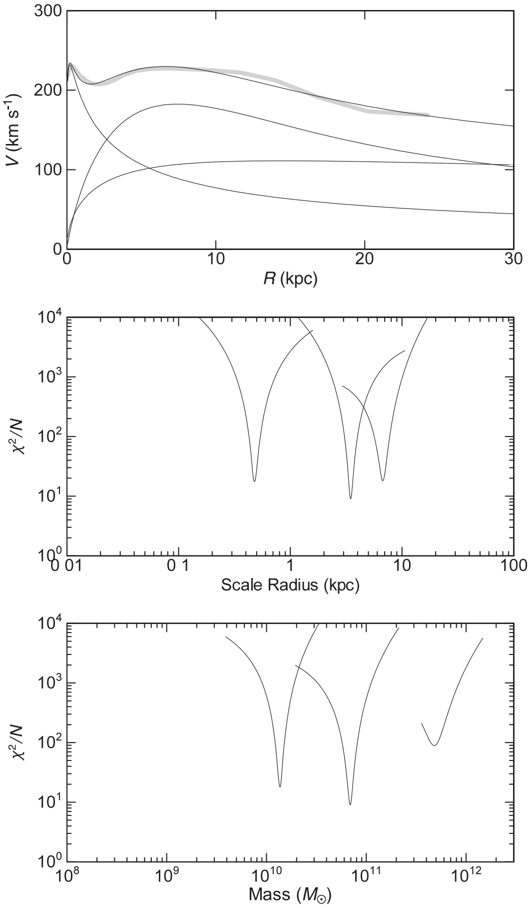

Fig. 30. Rotation curve and χ^2-fitting result for NGC 891 (top), the distribution of χ^2/N around the best-fitting scale radii (middle), and the masses (bottom) of the three components.

Table 8. Mean parameters for selected galaxies (Sofue 2016).

Bulge size	a_b	1.5 ± 0.2 kpc
Bulge mass	M_b	$2.3 \pm 0.4 \times 10^{10}\,M_\odot$
Disk size	a_d	3.3 ± 0.3 kpc
Disk mass	M_d	$5.7 \pm 1.1 \times 10^{10}\,M_\odot$
DH scale size	h	21.6 ± 3.9 kpc
DH mass within h	M_h	$22.3 \pm 7.3 \times 10^{10}\,M_\odot$
DH critical radius	R_{200}	193.7 ± 10.8 kpc
DH critical mass	M_{200}	$127.6 \pm 32.0 \times 10^{10}\,M_\odot$
Bulge+Disk	$M_\mathrm{b+d}$	$7.9 \pm 1.2 \times 10^{10}\,M_\odot$
Bulge+Disk+Halo	$M_\mathrm{Total}{}^*$	$135.6 \pm 32.0 \times 10^{10}\,M_\odot$
B+D / Halo ratio	$M_\mathrm{b+d}/M_{200}$	0.062 ± 0.018
B+D / Total ratio	$M_\mathrm{b+d}/M_\mathrm{Total}$	0.059 ± 0.016

$^*M_\mathrm{Total} = M_{200+\mathrm{b+d}}$.

The mass decomposition has also been applied extensively to spiral galaxies with relatively accurate rotation curves. It is a powerful tool for studying the relations of the scale radii and masses of the bulge and disk with those of the dark halo, which provides important information about the structure formation in the universe (Reyes et al. 2012; Behroozi et al. 2013; Miller et al. 2014).

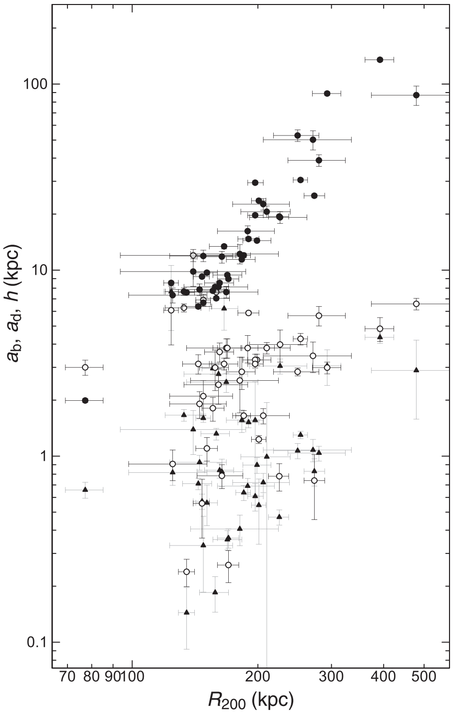

Fig. 31. Size–size relations for dark halo critical radius for (R_{200}, a_b) (triangles), (R_{200}, a_d) (open circles), and (R_{200}, h) (black dots) (Sofue 2016).

Decomposition has been applied to galaxies as compiled in figure 14 (Sofue 2016) by adopting the de Vaucouleurs, exponential, and NFW density profiles for the bulge, disk, and dark halo, respectively. The best-fitting values were obtained by applying the least-χ^2 method for M_b, a_b, M_d, a_d, ρ_0, and h. The critical dark halo radius, R_{200}, critical mass, M_{200}, as well as the mass, M_h, enclosed within the scale radius h, were also calculated:

$$M_{200} = 200\rho_c \frac{4\pi}{3} R_{200}^3, \tag{67}$$

where

$$\rho_c = 3H_0^2/(8\pi G), \tag{68}$$

with $H_0 = 72\,\mathrm{km\,s^{-1}\,Mpc^{-1}}$ being the Hubble constant.

Figure 30 shows examples of rotation curves and fitting result for NGC 891. The figure also shows the variation of χ^2 values plotted against the parameters. Applying a selection criterion, the fitting was obtained for 43 galaxies among the compiled samples in figure 14, and the mean values of the results are shown in table 8.

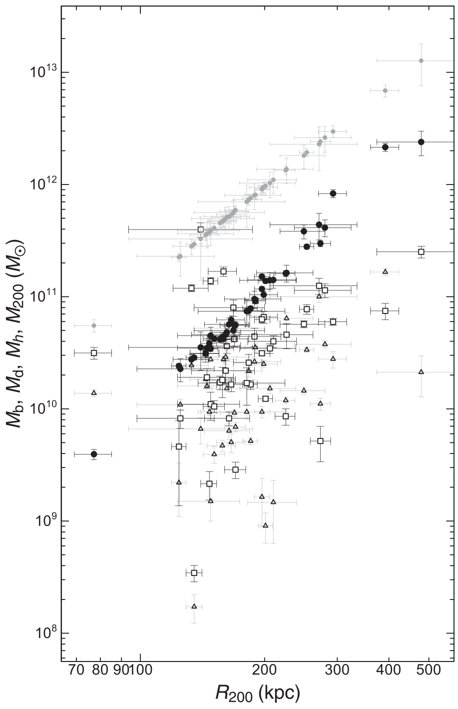

Fig. 32. Size–mass relations for (R_{200}, M_b) (triangles); (R_{200}, M_d) (rectangles); (R_{200}, M_h) (black dots); and (R_{200}, M_{200}) (small gray dots), showing the trivial relation by definition of the critical mass.

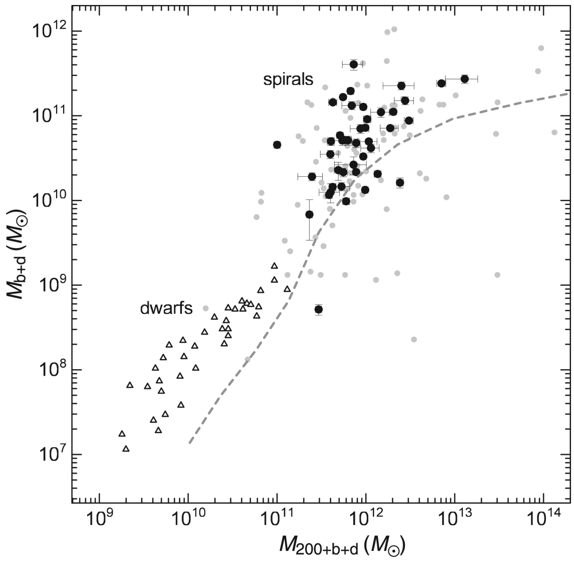

Fig. 33. M_{b+d}–$M_{200+b+d}$ relation compared with the stellar mass–total mass relation for dwarf galaxies (triangles: Miller et al. 2014) and simulation + photometry (dashed gray line: Behroozi et al. 2013). Black dots are the selected galaxies with reasonable fitting results, while small gray dots as well as black dots show non-weighted results from automatic decomposition of all rotation curves.

4.4.2 Size and mass fundamental relations

Correlations among the deconvolved parameters are useful for investigating the fundamental relations of dynamical properties of the mass components (e.g., Vogt et al. 2004a, 2004b). Figure 31 shows the size–size relations, where the scale radii a_b, a_d, and h are plotted against the critical radius R_{200} for the compiled nearby galaxies (Sofue 2016). It is shown that the bulge, disk, and halo scale radii are positively correlated with R_{200}. Note that the tight correlation between h and R_{200} includes the trivial internal relation due to the definition of the two parameters connected by ρ_0 through equation (67).

Figure 32 shows the size–mass relations, where the component masses, $M_{\rm b}$, $M_{\rm d}$, $M_{\rm h}$, and M_{200} are plotted against the critical dark halo radius R_{200}. The masses are positively correlated with the halo size. Note the trivial correlation showing the definition of the relation between R_{200} and M_{200}.

Figure 33 shows the bulge + disk mass, $M_{\rm b+d}$, plotted against total mass, $M_{200+\rm b+d} = M_{200} + M_{\rm b+d}$. In the figure we also plot photometric luminous mass and virial mass obtained for dwarf galaxies by Miller et al. (2014). Also is compared a cosmological simulation by Behroozi, Wechsler, and Conroy (2013). The simulation is in agreement in its shape with the plots for spiral and dwarf galaxies. The shape of simulated relation is consistent with the present dynamical observations, while the absolute values of $M_{\rm b+d}$ are greater than the simulated values by a factor of three. Solving the discrepancy may refine the cosmological models and will be a subject for the future.

The obtained correlations between the size and mass are the dynamical manifestation of the well-established luminosity–size relation by optical and infrared photometry (de Jong & Lacey 2000; Graham & Worley 2008; Simard et al. 2011). It is interesting to notice that a similar size–mass relation is found for dark halos.

The size–mass correlations can be fitted with straight lines on the log–log planes using the least-squares fitting. Measuring the mass and scale radii in units of $M_\odot$ and kpc, respectively, we have size–mass relations for the disk and dark halo of

$$\log_{10} M_{\rm d} = (9.89 \pm 0.23) + (1.38 \pm 0.41) \log_{10} a_{\rm d}, \qquad (69)$$

$$\log_{10} M_{\rm h} = (9.26 \pm 0.52) + (1.45 \pm 0.43) \log_{10} h. \qquad (70)$$

However, the relation for the bulge is too diverged to be fitted with a line.

The size–mass relation for the disk agrees with the luminosity–size relation obtained by Simard et al. (2011). It is found that the relations for the disk and dark halo can be represented by a single (common) relation:

$$\log_{10} M_i = (10.18 \pm 0.24) + (1.38 \pm 0.21) \log_{10} a_i, \qquad (71)$$

where $M_i = M_{\rm b+d}$ or M_{200} in $10^{10}\,M_\odot$ and $a_i = a_{\rm d}$ or h in kpc. This simple equation leads to a relation between the bulge + disk mass and halo mass. Their ratio, $M_{\rm b+d}/M_{200}$, approximately represents the baryonic fraction, and is expressed by the ratio of the scale radius of disk to that of halo as

$$M_{\rm b+d}/M_{200} \simeq (a_{\rm d}/h)^{1.38}. \qquad (72)$$

For the mean values of $\langle a_{\rm d}\rangle = 3.3$ kpc and $\langle h\rangle = 21.6$ kpc, we obtain $M_{\rm b+d}/M_{200} \sim 0.07$.

5 Concluding remarks

5.1 Summary

We reviewed the methods to observe and determine rotation curves of the Milky Way and of spiral galaxies. Rotation characteristics of spiral galaxies and their mass distributions were shown to be similar to those of other various types of galaxies. The dynamical structures are, thus, universal to Sa–Sc galaxies. The Milky Way exhibits representative universal characteristics, from the central black hole to the outermost dark halo.

Major methods to derive the dynamical mass distribution in disk galaxies were described, and some results were presented. The direct method does not employ any galactic models or functional forms, but simply computes the mass distribution. On the other hand, the decomposition method yields fundamental parameters representing the bulge, disk, and dark halo individually. The decomposition is thus a convenient method for discussing the fundamental structures composed of a bulge, a disk, and a dark halo. The fitting dynamical parameters were also useful for statistical correlation analyses such as the size–mass and mass–mass relations, which provide fundamental information on the formation and evolution scenarios of galaxies in the universe.

5.2 Achievements in past decades and in the future

In our previous review (Sofue & Rubin 2001) various advances were expected for the future rotation curve studies, thanks principally to instrumental developments. We summarize and evaluate the progress in past decades.

5.2.1 Extinction-free rotation kinematics in the central region

This has been achieved extensively using CO line spectroscopy and imaging, and will be achieved in an ultimate way using the ALMA with higher spatial ($0\farcs01$) resolution. Spectroscopy with 8 and 10 m class optical/infrared telescopes using infrared spectral lines such as Br γ was anticipated, although the progress does not seem fast, and no outstanding advances have been achieved.

5.2.2 VLBI astrometry

The VERA observations have successfully achieved high-resolution astrometric measurements of parallactic distances, positions, proper motions, and radial velocities for a number of maser sources in the Milky Way. The observations resulted in a series of special volumes in the Publications of the Astronomical Society of Japan (Honma et al. 2015, and the literature therein). Many new aspects have been learned with regard to the details of the 3D kinematics of the Galaxy, which include the new values of (R_0, V_0), non-circular motions related to the density waves and bars. The SKA (Square-Kilometer Array) will be a future, probably more powerful, tool for trigonometric determination of the Galactic rotation curve and dynamics even by simply extending the method employed by VERA.

5.2.3 High-redshift rotation curves

Thanks to the increase of aperture and sensitivity of telescopes, particularly using the Hubble Space Telescope and ground-based 8–10 m telescopes, galaxies at cosmological distances are becoming routine targets for rotation curve observations. Tens of galaxies at high redshifts have their rotation velocities measured. The data are still not sensitive enough to be compared with those for the nearby galaxies. The global rotation curve shapes seem to be similar already at $z \sim 3$–5. Combined with cosmological simulations of structural formation and evolution, this would become one of the most popular fields in rotation curve study.

However, the inner rotation curves representing the bulge and central massive objects are still not resolved at high redshifts. As mentioned already, an angular resolution of $0.''01$ corresponds only to ∼200 pc at $z \gtrsim 2$. Higher resolution instruments are desired for more detailed study of the bulge and black hole formation, which is one of the major events in primeval galaxies.

5.2.4 Method of analysis

Rotation curves presented in this review have been derived simply using popular methods such as PV tracing and tilted ring methods. The PV iteration method was also applied, although only for a few cases.

The development of sophisticated iteration methods of 2D and 3D velocity fields in order to produce more accurate rotation curves has been anticipated. However, not much advance has been made in recent decades. More sophisticated methods will lead to more tightly constrained mass deconvolution, and the precise distributions of the stellar and dark matter masses.

5.2.5 Dark halos

Dark halos are one of the major topics in the fields of not only galaxy dynamics and kinematics but also the structure formation and evolution in the expanding universe. As to the Milky Way and M 31, it has been shown that their rotation curves, and hence the dark matter halos, seem to be merged at halfway between the two. Both galaxies showed declining rotation at radii larger than $R \sim 50$ kpc. Their outermost rotation curves are not flat anymore and are not well-fitted with the current pseudo-isothermal models, but they seem to be better approximated by the NFW model. However, it may be mentioned that the isothermal model is simple and is enough to represent dark halos up to ∼30–50 kpc, beyond which it is still difficult to obtain rotation curves in most of observed galaxies.

Thus, the measurements of the dynamical mass of dark halos in most galaxies are limited to radii of ∼20–30 kpc, where it is difficult to discriminate the halo models. Measurements at larger radii, up to ∼100 kpc, for a greater number of galaxies are crucial for conclusive comparison with the cosmological scenarios of structural formation.

Dark matter density in the solar neighborhood has been determined in the range around ∼0.2–0.4 GeV cm^{-3}. The physical property of the dark matter in view of elementary particle physics would be clarified when direct detection in the laboratory is achieved. Also, indirect detection toward the Sun and the Galactic Center are proposed and partly performed. Although at the moment there appears to be no firm detection reported, this would be the fundamental field in experimental physics in the near future.

5.2.6 Massive black holes

Co-evolution of the spheroidal component and central supermassive black hole is a standard scenario in the structural evolution of galaxies based on the observational fact that black hole mass is positively correlated with the spheroidal mass in observed galaxies. This topic was, however, not reviewed in this paper, mainly because of an insufficient sample of galaxies with both the black hole mass and the detailed rotation curve around the nuclei. Such a study would be a promising subject for high-resolution submillimeter spectroscopy using ALMA and infrared spectroscopy with large-aperture telescopes, including the Thirty Meter Telescope (TMT).

5.2.7 Activities

Many of galaxies with well-defined rotation curves as discussed in this review are known to be galaxies that possess various active components, such as starbursts, outflows, jets, and/or active galactic nuclei. However, there has been no clear correlation analysis among these activities and the galactic mass distribution. It could be a subject for a more detailed comparison study with careful inspection of the individual curves and mass structures, categorizing the curves into those with and without such activities. It may be related to central bars by which the gas is accumulated to the nuclei, and hence the correlation of the rotation curves of barred and non-barred galaxies.

5.2.8 Star formation

Correlation analysis of general star-forming activity in the disk with the rotation curves and mass structure would be a fundamental subject related to ISM physics in galaxies. It is a known relation that low surface brightness galaxies are generally slowly rotating and less massive. On the other hand, high-velocity rotators, usually of late-types such as Sa and S0, show that their major star formation activity was over in the far past. In Sb and Sc galaxies, the star formation rate is not necessarily controlled by the mass structure, but rather related to spiral arms and/or bars, or to environmental effects such as interaction with other galaxies.

The relation between mass structure and star-forming activity is, therefore, not well studied from observations of galaxies at the present epoch (redshift $z \simeq 0$). This is readily shown by the observed constant M/L ratio among galaxies, where M/L ratios do not represent star-forming activity. Direct relation between the mass structure and the star formation would be studied by rotation curve analysis of high-redshift galaxies during their major star formation.

5.2.9 Bars and spiral arms

In the current rotation curve studies the bar/non-bar discrimination has not necessarily been the major subject, for the reason raised in section 2 (table 2). In this article, we reviewed rotation curves based on the assumption that the galactic rotation is circular and axisymmetric. Therefore, we did not touch upon spiral arms or bars in detail.

The separation of arm- and bar-related parameters is still difficult even though the data get wider, deeper, and more accurate. The number of parameters required to reach a unique result is still too large. The difficulty has not been solved even by numerical simulations.

Some new technique to analyze the mass distribution and motion in arms and bars directly is desired. More detailed inspection, probably in a more sophisticated way, of spectroscopic 2D and 3D data cubes of a larger number of galaxies, particularly data obtained with facilities such as 2D Fabry–Perot instruments, velocity cubes in H I and CO, or using more advanced interferometers like SKA and ALMA, would lead to a deeper insight into mass structures of galaxies including bars and spiral arms.

References

Aaronson, M., & Mould, J. 1986, ApJ, 303, 1

Amram, P., Marcelin, M., Balkowski, C., Cayatte, V., Sullivan, W. T., III, & Le Coarer, E., 1994, A&AS, 103, 5

Appleton, P. N., Foster, P. A., & Davies, R. D. 1986, MNRAS, 221, 393

Arimoto, N., Sofue, Y., & Tsujimoto, T. 1996, PASJ, 48, 275

Athanassoula, E. 1992, MNRAS, 259, 328

Battinelli, P., Demers, S., Rossi, C., & Gigoyan, K. S. 2013, Astrophysics, 56, 68

Begeman, K. G. 1989, A&A, 223, 47

Begeman, K. G., Broeils, A. H., & Sanders, R. H. 1991, MNRAS, 249, 523

Behroozi, P. S., Wechsler, R. H., & Conroy, C. 2013, ApJ, 770, 57

Bershady, M. A., Verheijen, M. A. W., Swaters, R. A., Andersen, D. R., Westfall, K. B., & Martinsson, T. 2010a, ApJ, 716, 198

Bershady, M. A., Verheijen, M. A. W., Westfall, K. B., Andersen, D. R., Swaters, R. A., & Martinsson, T. 2010b, ApJ, 716, 234

Bertola, F., Cappellari, M., Funes, S. J., José, G., Corsini, E. M., Pizzella, A., & Beltrán, J. C. V. 1998, ApJ, 509, L93

Bhattacharjee, P., Chaudhury, S., & Kundu, S. 2014, ApJ, 785, 63

Bhattacharjee, P., Chaudhury, S., Kundu, S., & Majumdar, S. 2013, Phys. Rev. D, 87, 083525

Binney, J., Gerhard, O. E., Stark, A. A., Bally, J., & Uchida, K. I. 1991, MNRAS, 252, 210

Binney, J., & Tremaine, S. 1987, in Galactic Dynamics (Princeton, NJ: Princeton Univ. Press)

Blais-Ouellette, S., Amram, P., & Carignan, C. 2001, AJ, 121, 1952

Blais-Ouellette, S., Amram, P., Carignan, C., & Swaters, R. 2004, A&A, 420, 147

Blitz, L., Fich, M., & Stark, A. A. 1982, ApJS, 49, 183

Blitz, L., & Lada, C. J. 1979, ApJ, 227, 152

Bobylev, V. V. 2013, Astron. Lett., 39, 95

Bobylev, V. V., & Bajkova, A. T. 2015, Astron. Lett., 41, 473

Bosma, A. 1981a, AJ, 86, 1791

Bosma, A. 1981b, AJ, 86, 1825

Bouché, N., Carfantan, H., Schroetter, I., Michel-Dansac, L., & Contini, T. 2015, AJ, 150, 92

Bovy, J., & Tremaine, S. 2012, ApJ, 756, 89

Broeils, A. H. 1992, A&A, 256, 19

Burkert, A. 1995, ApJ, 447, L25

Burton, W. B., & Gordon, M. A. 1978, A&A, 63, 7

Burton, W. B., & Liszt, H. S. 1993, A&A, 274, 765

Buta, R., Purcell, G. B., Cobb, M. L., Crocker, D. A., Rautiainen, P., & Salo, H. 1999, AJ, 117, 778

Carignan, C. 1985, ApJ, 299, 59

Carignan, C., & Beaulieu, S. 1989, ApJ, 347, 760

Carignan, C., Chemin, L., Huchtmeier, W. K., & Lockman, F. J. 2006, ApJ, 641, L109

Carignan, C., & Freeman, K. C. 1985, ApJ, 294, 494

Carignan, C., & Puche, D. 1990a, AJ, 100, 394

Carignan, C., & Puche, D. 1990b, AJ, 100, 641

Chemin, L., Carignan, C., & Foster, T. 2009, ApJ, 705, 1395

Ciotti, L. 1991, A&A, 249, 99

Clemens, D. P. 1985, ApJ, 295, 422

Corradi, R. L. M., Boulesteix, J., Bosma, A., Amram, P., & Capaccioli, M. 1991, A&A, 244, 27

Courteau, S. 1997, AJ, 114, 2402
Daigle, O., Carignan, C., Amram, P., Hernandez, O., Chemin, L., Balkowski, C., & Kennicutt, R. 2006, MNRAS, 367, 469
Dame, T. M., Hartmann, D., & Thaddeus, P. 2001, ApJ, 547, 792
de Blok, W. J. G. 2005, ApJ, 634, 227
de Blok, W. J. G., & Bosma, A. 2002, A&A, 385, 816
de Blok, W. J. G., McGaugh, S. S., & Rubin, V. C. 2001, AJ, 122, 2396
de Blok, W. J. G., McGaugh, S. S., & van der Hulst, J. M. 1996, MNRAS, 283, 18
de Blok, W. J. G., Walter, F., Brinks, E., Trachternach, C., Oh, S.-H., & Kennicutt, R. C., Jr, 2008, AJ, 136, 2648
de Jong, R. S., & Lacey, C. 2000, ApJ, 545, 781
de Vaucouleurs, G. 1958, ApJ, 128, 465
Dehnen, W., & Binney, J. 1998, MNRAS, 294, 429
Demers, S., & Battinelli, P. 2007, A&A, 473, 143
Dicaire, I., et al. 2008, MNRAS, 385, 553
DiTeodoro, E. M., & Fraternali, F. 2015, MNRAS, 451, 3021
Epinat, B., et al. 2012, A&A, 539, A92
Erb, D. K., Shapley, A. E., Steidel, C. C., Pettini, M., Adelberger, K. L., Hunt, M. P., Moorwood, A. F. M., & Cuby, J.-G. 2003, ApJ, 591, 101
Erroz-Ferrer, S., et al. 2012, MNRAS, 427, 2938
Feast, M., & Whitelock, P. 1997, MNRAS, 291, 683
Ferrarese, L., & Ford, H. C. 1999, ApJ, 515, 583
Fich, M., Blitz, L., & Stark, A. A. 1989, ApJ, 342, 272
Fich, M., & Tremaine, S. 1991, ARA&A, 29, 409
Forbes, D. A. 1992, A&AS, 92, 583
Freeman, K. C. 1970, ApJ, 160, 811
Fridman, A. M., Afanasiev, V. L., Dodonov, S. N., Khoruzhii, O. V., Moiseev, A. V., Sil'chenko, O. K., & Zasov, A. V. 2005, A&A, 430, 67
Galazutdinov, G., Strobel, A., Musaev, F. A., Bondar, A., & Krełowski, J. 2015, PASP, 127, 126
Garrido, O., Marcelin, M., & Amram, P. 2004, MNRAS, 349, 225
Garrido, O., Marcelin, M., Amram, P., Balkowski, C., Gach, J. L., & Boulesteix, J. 2005, MNRAS, 362, 127
Garrido, O., Marcelin, M., Amram, P., & Boulesteix, J. 2002, A&A, 387, 821
Gentile, G., et al. 2015, A&A, 576, A57
Gentile, G., Salucci, P., Klein, U., & Granato, G. L. 2007, MNRAS, 375, 199
Genzel, R., et al. 2008, ApJ, 687, 59
Genzel, R., et al. 2011, ApJ, 733, 101
Genzel, R., Eckart, A., Ott, T., & Eisenhauer, F. 1997, MNRAS, 291, 219
Genzel, R., Eisenhauer, F., & Gillessen, S. 2010, Rev. Modern Phys., 82, 3121
Genzel, R., Hollenbach, D., & Townes, C. H. 1994, Rep. Prog. Phys., 57, 417
Genzel, R., Pichon, C., Eckart, A., Gerhard, O. E., & Ott, T. 2000, MNRAS, 317, 348
Ghez, A. M., et al. 2008, ApJ, 689, 1044
Ghez, A. M., Klein, B. L., Morris, M., & Becklin, E. E. 1998, ApJ, 509, 678
Ghez, A. M., Salim, S., Hornstein, S. D., Tanner, A., Lu, J. R., Morris, M., Becklin, E. E., & Duchêne, G. 2005, ApJ, 620, 744
Gillessen, S., Eisenhauer, F., Trippe, S., Alexander, T., Genzel, R., Martins, F., & Ott, T. 2009, ApJ, 692, 1075
Graham, A. W., & Worley, C. C. 2008, MNRAS, 388, 1708
Greenhill, L. J., Gwinn, C. R., Antonucci, R., & Barvainis, R. 1996, ApJ, 472, L21
Haschick, A. D., Baan, W. A., Schneps, M. H., Reid, M. J., Moran, J. M., & Guesten, R. 1990, ApJ, 356, 149
Héraudeau, P., & Simien, F. 1997, A&A, 326, 897
Hernandez, O., Carignan, C., Amram, P., Chemin, L., & Daigle, O. 2005, MNRAS, 360, 1201
Herrnstein, J. R., et al. 1999, Nature, 400, 539
Hlavacek-Larrondo, J., Carignan, C., Daigle, O., de Denus-Baillargeon, M.-M., Marcelin, M., Epinat, B., & Hernandez, O. 2011a, MNRAS, 411, 71
Hlavacek-Larrondo, J., Marcelin, M., Epinat, B., Carignan, C., de Denus-Baillargeon, M.-M., Daigle, O., & Hernandez, O. 2011b, MNRAS, 416, 509
Honma, M., et al. 2007, PASJ, 59, 889
Honma, M., et al. 2012, PASJ, 64, 136
Honma, M., Nagayama, T., & Sakai, N. 2015, PASJ, 67, 70
Honma, M., & Sofue, Y. 1997, PASJ, 49, 453
Hunter, J. H., Jr, & Cottesman, S. T., 1996, ASPC, 91, 398
Irwin, J. A., & Sofue, Y. 1992, ApJ, 396, L75
Jenkins, A., & Binney, J. 1994, MNRAS, 270, 703
Jobin, M., & Carignan, C. 1990, AJ, 100, 648
Józsa, G. I. G., Kenn, F., Klein, U., & Oosterloo, T. A. 2007, A&A, 468, 731
Kamphuis, J., & Briggs, F. 1992, A&A, 253, 335
Kelson, D. D., Illingworth, G. D., van Dokkum, P. G., & Franx, M. 2000, ApJ, 531, 159
Kent, S. M. 1986, AJ, 91, 1301
Kent, S. M., Dame, T. M., & Fazio, G. 1991, ApJ, 378, 131
Kerr, F. J., & Lynden-Bell, D. 1986, MNRAS, 221, 1023
Kim, S., Staveley-Smith, L., Dopita, M. A., Freeman, K. C., Sault, R. J., Kesteven, M. J., & McConnell, D. 1998, ApJ, 503, 674
Kong, D. L., & Zhu, Z. 2008, Acta Astron. Sin., 49, 224
Kormendy, J., & Freeman, K. C. 2016, ApJ, 817, 84
Kormendy, J., & Ho, L. C. 2013, ARA&A, 51, 511
Kormendy, J., & Richstone, D. 1995, ARA&A, 33, 581
Kormendy, J., & Westpfahl, D. J. 1989, ApJ, 338, 752
Krabbe, A., Colina, L., Thatte, N., & Kroker, H. 1997, ApJ, 476, 98
Kuno, N., Nishiyama, K., Nakai, N., Sorai, K., Vila-Vilaró, B., & Handa, T. 2000, PASJ, 52, 775
Kwee, K. K., Muller, C. A., & Westerhout, G. 1954, Bull. Astron. Inst. Ned., 12, 211
Lake, G., Schommer, R. A., & van Gorkom, J. H. 1990, AJ, 99, 547
Law, D. R., Steidel, C. C., Erb, D. K., Larkin, J. E., Pettini, M., Shapley, A. E., & Wright, S. A. 2009, ApJ, 697, 2057
Lindqvist, M., Habing, H. J., & Winnberg, A. 1992, A&A, 259, 118
López-Corredoira, M. 2014, A&A, 563, A128
Makarov, D. I., Burenkov, A. N., & Tyurina, N. V. 2001, Astron. Lett., 27, 213
Makarov, D. I., Karachentsev, I. D., Tyurina, N. V., & Kaisin, S. S. 1997, Astron. Lett., 23, 445

Márquez, I., et al. 2004, A&A, 416, 475
Márquez, I., Masegosa, J., Moles, M., Varela, J., Bettoni, D., & Galletta, G. 2002, A&A, 393, 389
Martinsson, T. P. K., Verheijen, M. A. W., Westfall, K. B., Bershady, M. A., Andersen, D. R., & Swaters, R. A. 2013a, A&A, 557, A131
Martinsson, T. P. K., Verheijen, M. A. W., Westfall, K. B., Bershady, M. A., Schechtman-Rook, A., Andersen, D. R., & Swaters, R. A. 2013b, A&A, 557, A130
Masters, K. L., Crook, A., Hong, T., Jarrett, T. H., Koribalski, B. S., Macri, L., Springob, C. M., & Staveley-Smith, L. 2014, MNRAS, 443, 1044
Masters, K. L., Springob, C. M., & Huchra, J. P. 2008, AJ, 135, 1738
Mathewson, D. S., & Ford, V. L. 1996, ApJS, 107, 97
Mathewson, D. S., Ford, V. L., & Buchhorn, M. 1992, ApJS, 81, 413
Matsunaga, N., Kawadu, T., Nishiyama, S., Nagayama, T., Hatano, H., Tamura, M., Glass, I. S., & Nagata, T. 2009, MNRAS, 399, 1709
McGaugh, S. S., Rubin, V. C., & de Blok, W. J. G. 2001, AJ, 122, 2381
Merrifield, M. R. 1992, AJ, 103, 1552
Mignard, F. 2000, A&A, 354, 522
Miller, S. H., Ellis, R. S., Newman, A. B., & Benson, A. 2014, ApJ, 782, 115
Miyamoto, M., & Nagai, R. 1975, PASJ, 27, 533
Miyoshi, M., Moran, J., Herrnstein, J., Greenhill, L., Nakai, N., Diamond, P., & Inoue, M. 1995, Nature, 373, 127
Nakai, N., Inoue, M., & Miyoshi, M. 1993, Nature, 361, 45
Nakanishi, H., et al. 2015, PASJ, 67, 68
Nakanishi, H., & Sofue, Y. 2003, PASJ, 55, 191
Nakanishi, H., & Sofue, Y. 2006, PASJ, 58, 847
Nakanishi, H., & Sofue, Y. 2016, PASJ, 68, 5
Navarro, J. F., Frenk, C. S., & White, S. D. M. 1996, ApJ, 462, 563
Navarro, J. F., Frenk, C. S., & White, S. D. M. 1997, ApJ, 490, 493
Noordermeer, E. 2008, MNRAS, 385, 1359
Noordermeer, E., van der Hulst, J. M., Sancisi, R., Swaters, R. A., & van Albada, T. S. 2005, A&A, 442, 137
Noordermeer, E., van der Hulst, J. M., Sancisi, R., Swaters, R. S., & van Albada, T. S. 2007, MNRAS, 376, 1513
Oikawa, S., & Sofue, Y. 2014, PASJ, 66, 77
Oka, T., Hasegawa, T., Sato, F., Tsuboi, M., & Miyazaki, A. 1998, ApJS, 118, 455
Olling, R. P. 1996, AJ, 112, 457
Olling, R. P., & Dehnen, W. 2003, ApJ, 599, 275
Olling, R. P., & Merrifield, M. R. 1998, MNRAS, 297, 943
Oort, J. H. 1965, in Stars and Stellar Systems, Vol. 5, Galactic Structure, ed.Blaauw, A., & Schmidt, M. (Chicago: University Chicago Press), 455
Oort, J. H., Kerr, F. J., & Westerhout, G. 1958, MNRAS, 118, 379
Östlin, G., Amram, P., Masegosa, J., Bergvall, N., & Boulesteix, J. 1999, A&AS, 137, 419
Pato, M., & Iocco, F. 2015, ApJ, 803, L3
Pato, M., Iocco, F., & Bertone, G. 2015, JCAP, 12, 001
Persic, M., & Salucci, P. 1990, MNRAS, 247, 349
Persic, M., & Salucci, P. 1991, ApJ, 368, 60
Persic, M., & Salucci, P. 1995, ApJS, 99, 501
Persic, M., Salucci, P., & Stel, F. 1996, MNRAS, 281, 27
Piffl, T., et al. 2014, MNRAS, 445, 3133
Puche, D., Carignan, C., & Bosma, A. 1990, AJ, 100, 1468
Puche, D., Carignan, C., & van Gorkom, J. H. 1991a, AJ, 101, 456
Puche, D., Carignan, C., & Wainscoat, R. J. 1991b, AJ, 101, 447
Randriamampandry, T. H., Combes, F., Carignan, C., & Deg, N. 2015, MNRAS, 454, 3743
Regan, M. W., & Vogel, S. N. 1994, ApJ, 434, 536
Reid, M. J. 1993, ARA&A, 31, 345
Reid, M. J., et al. 2009, ApJ, 700, 137
Reyes, R., Mandelbaum, R., Gunn, J. E., Nakajima, R., Seljak, U., & Hirata, C. M. 2012, MNRAS, 425, 2610
Richards, E. E., et al. 2015, MNRAS, 449, 3981
Richstone, D., et al. 1998, Nature, 395, A14
Roberts, M. S. 1966, ApJ, 144, 639
Robertson, B. E., & Bullock, J. S. 2008, ApJ, 685, L27
Roeser, S., Demleitner, M., & Schilbach, E. 2010, AJ, 139, 2440
Roscoe, D. F. 1999, A&A, 343, 788
Rots, A. H., Bosma, A., van der Hulst, J. M., Athanassoula, E., & Crane, P. C. 1990, AJ, 100, 387
Rubin, V. C., Burstein, D., Ford, W. K., Jr, & Thonnard, N., 1985, ApJ, 289, 81
Rubin, V. C., Ford, W. K., Jr, Thonnard, N., & Burstein, D. 1982a, ApJ, 261, 439
Rubin, V. C., Hunter, D. A., & Ford, W. K., Jr, 1991, ApJS, 76, 153
Rubin, V. C., Kenney, J. D. P., & Young, J. S. 1997, AJ, 113, 1250
Rubin, V. C., Thonnard, N. T., & Ford, W. K., Jr. 1982b, AJ, 87, 477
Rubin, V. C., Waterman, A. H., & Kenney, J. D. P. 1999, AJ, 118, 236
Ryder, S. D., Zasov, A. V., McIntyre, V. J., Walsh, W., & Sil'chenko, O. K. 1998, MNRAS, 293, 411
Sakai, N., et al. 2015, PASJ, 67, 69
Sakai, N., Honma, M., Nakanishi, H., Sakanoue, H., Kurayama, T., Shibata, K. M., & Shizugami, M. 2012, PASJ, 64, 108
Salucci, P., & Frenk, C. S. 1989, MNRAS, 237, 247
Salucci, P., Lapi, A., Tonini, C., Gentile, G., Yegorova, I., & Klein, U. 2007, MNRAS, 378, 41
Salucci, P., Nesti, F., Gentile, G., & Frigerio Martins, C. 2010, A&A, 523, A83
Sawada-Satoh, S., Inoue, M., Shibata, K. M., Kameno, S., Migenes, V., Nakai, N., & Diamond, P. J. 2000, PASJ, 52, 421
Scarano, S., Madsen, F. R. H., Roy, N., & Lépine, J. R. D. 2008, MNRAS, 386, 963
Schombert, J. M., & Bothun, G. D. 1988, AJ, 95, 1389
Schombert, J. M., Bothun, G. D., Schneider, S. E., & McGaugh, S. S. 1992, AJ, 103, 1107
Sérsic, J. L. 1968, Atlas de Galaxias Australes (Cordoba: Observatorio Astronomico)
Shapiro, K. L., et al. 2008, ApJ, 682, 231
Shetty, R., Vogel, S. N., Ostriker, E. C., & Teuben, P. J. 2007, ApJ, 665, 1138
Simard, L., Mendel, J. T., Patton, D. R., Ellison, S. L., & McConnachie, A. W. 2011, ApJS, 196, 11

Simard, L., & Pritchet, C. J. 1998, ApJ, 505, 96
Sofue, Y. 1996, ApJ, 458, 120
Sofue, Y. 1997, PASJ, 49, 17
Sofue, Y. 1999, PASJ, 51, 445
Sofue, Y. 2011, PASJ, 63, 813
Sofue, Y. 2012, PASJ, 64, 75
Sofue, Y. 2013a, in Planets, Stars and Stellar Systems, Vol. 5, Galactic Structure and Stellar Popuration, ed. G. Gilmore (Dordrecht: Springer), ch. 19
Sofue, Y. 2013b, PASJ, 65, 118
Sofue, Y. 2015, PASJ, 67, 75
Sofue, Y. 2016, PASJ, 68, 2
Sofue, Y., Honma, M., & Omodaka, T. 2009, PASJ, 61, 227
Sofue, Y., & Irwin, J. A. 1992, PASJ, 44, 353
Sofue, Y., Koda, J., Nakanishi, H., & Onodera, S. 2003, PASJ, 55, 59
Sofue, Y., & Nakanishi, H. 2016, PASJ, 68, 63
Sofue, Y., & Rubin, V. 2001, ARA&A, 39, 137
Sofue, Y., Tomita, A., Tutui, Y., Honma, M., & Takeda, Y. 1998, PASJ, 50, 427
Sofue, Y., Tutui, Y., Honma, M., & Tomita, A. 1997, AJ, 114, 2428
Sofue, Y., Tutui, Y., Honma, M., Tomita, A., Takamiya, T., Koda, J., & Takeda, Y. 1999, ApJ, 523, 136
Spano, M., Marcelin, M., Amram, P., Carignan, C., Epinat, B., & Hernandez, O. 2008, MNRAS, 383, 297
Spekkens, K., & Sellwood, J. A. 2007, ApJ, 664, 204
Swaters, R. A., Madore, B. F., & Trewhella, M. 2000, ApJ, 531, L107
Swaters, R. A., Sancisi, R., van Albada, T. S., & van der Hulst, J. M. 2009, A&A, 493, 871
Takamiya, T., & Sofue, Y. 2000, ApJ, 534, 670
Takamiya, T., & Sofue, Y. 2002, ApJ, 576, L15
Takase, B. 1957, PASJ, 9, 16
Tecza, M., Thatte, N., & Maiolino, R. 2001, in IAU Symp. 205, Galaxies and their Constituents at the Highest Angular Resolution, ed. R. T. Schilizzi et al. (San Francisco: ASP), 216
Trotter, A. S., Greenhill, L. J., Moran, J. M., Reid, M. J., Irwin, J. A., & Lo, K.-Y. 1998, ApJ, 495, 740
Trujillo, I., Asensio Ramos, A., Rubiño-Martín, J. A., Graham, A. W., Aguerri, J. A. L., Cepa, J., & Gutiérrez, C. M. 2002, MNRAS, 333, 510
Tully, R. B., & Fisher, J. R. 1977, A&A, 54, 661
van der Marel, R. P., Rix, H. W., Carter, D., Franx, M., White, S. D. M., & de Zeeuw, T. 1994, MNRAS, 268, 521
van der Wel, A., & van der Marel, R. P. 2008, ApJ, 684, 260
van Gorkom, J. H., van der Hulst, J. M., Haschick, A. D., & Tubbs, A. D. 1990, AJ, 99, 1781
Vaughan, J. M. 1989, The Fabry-Perot Interferometer: History, Theory, Practice and Applications (Boca Raton, FL: CRC Press)
Vogel, S. N., Rand, R. J., Gruendl, R. A., & Teuben, P. J. 1993, PASP, 105, 666
Vogt, N. P., et al. 1997, ApJ, 479, L121
Vogt, N. P., Forbes, D. A., Phillips, A. C., Gronwall, C., Faber, S. M., Illingworth, G. D., & Koo, D. C. 1996, ApJ, 465, L15
Vogt, N. P., Haynes, M. P., Giovanelli, R., & Herter, T. 2004a, AJ, 127, 3325
Vogt, N. P., Haynes, M. P., Herter, T., & Giovanelli, R. 2004b, AJ, 127, 3273
Vogt, N. P., Herter, T., Haynes, M. P., & Courteau, S. 1993, ApJ, 415, L95
Watson, W. D., & Wallin, B. K. 1994, ApJ, 432, L35
Weber, M., & de Boer, W. 2010, A&A, 509, A25
Weiner, B. J., & Williams, T. B. 1996, AJ, 111, 1156
Westfall, K. B., Andersen, D. R., Bershady, M. A., Martinsson, T. P. K., Swaters, R. A., & Verheijen, M. A. W. 2014, ApJ, 785, 43
Whitmore, B. C., McElroy, D. B., & Schweizer, F. 1987, ApJ, 314, 439